

Variations in the density distribution of the Io plasma torus as seen by radio occultations on Juno Perijoves 3, 6, and 8

Phillip H. Phipps¹, Paul Withers^{1,2}, Dustin R. Buccino³, Yu-Ming Yang³, Marzia Parisi³

¹Department of Astronomy, Boston University, Boston, MA, USA.

²Center for Space Physics, Boston University, Boston, MA, USA.

³Jet Propulsion Laboratory, California Institute of Technology, Pasadena, CA, USA.

Key Points:

- Io plasma torus total electron content profiles are derived from Juno Perijoves 3, 6, and 8.
- Torus locations are displaced from nominal centrifugal equator.
- Peak total electron content and scale height vary with System III longitude.

12 **Abstract**

13 The atmosphere of the Jovian satellite Io is constantly being lost to the surrounding mag-
 14 netosphere of Jupiter. The material is ionized and then distributed by Jupiter's magnetic
 15 field into a torus around Jupiter called the Io plasma torus. This plasma affects radio
 16 signals as they propagate from the Juno spacecraft to Earth during the spacecraft's peri-
 17 jove passes. During Perijoves 3, 6, and 8 we determine the total electron content in the
 18 Io plasma torus using two-way tracking data from Juno. We find that the location of the
 19 torus is displaced from predictions that use the VIP4 offset tilted dipole approximation.
 20 The displacements are consistent with those found in ground-based observations. The
 21 peak total electron content and scale height are found for two different regions of the
 22 torus, the cold inner torus and a warmer torus beyond $5.5 R_J$. Properties of the cold torus
 23 vary appreciably with System III longitude, but properties of the torus beyond $5.5 R_J$ do
 24 not.

25 **1 Introduction**

26 The Galilean satellite Io orbits Jupiter in the plane of the planet's rotational equator
 27 at a distance of 5.9 Jupiter radii (R_J) with a period of 1.8 days (42 hours). Once neutral
 28 species that escape from Io's atmosphere enter the magnetosphere, they are ionized via
 29 electron impact and charge exchange [Thomas *et al.*, 2004]. The resultant plasma disperses
 30 outwards to fill the magnetosphere. However, dispersal is slow, occurring on timescales of
 31 weeks [Bagenal *et al.*, 2017a].

32 Plasma produced near Io is picked up by Jupiter's magnetic field and then trapped
 33 on a magnetic field-line. Jupiter's magnetic field is approximately dipolar, so these mag-
 34 netic field-lines effectively lie in a plane of fixed longitude. Trapped plasma is forced to
 35 rotate with Jupiter's rotational period of 10 hours, though the plasma slightly lags behind
 36 corotation with the magnetic field [Khurana *et al.*, 2004], which disperses plasma along
 37 the orbital path of slower-moving Io. In principle, plasma could drift out of the equato-
 38 rial plane whilst remaining on its magnetic field-line. However, Jupiter's rapid rotation
 39 forces plasma to the point of minimum centrifugal potential, which is the point on the
 40 field-line furthest from Jupiter's rotational axis [Hill *et al.*, 1974; Dessler, 1983; Khurana
 41 *et al.*, 2004]. For a dipole field aligned with the rotational axis, plasma remains trapped in
 42 the equatorial plane. The net result of trapping on a field line (dispersal of plasma along
 43 Io's orbital path) and centrifugal forces (confinement of plasma to the equatorial plane)
 44 is a torus of plasma. This torus of plasma is the most prominent feature in Jupiter's vast
 45 magnetosphere: the Io plasma torus (IPT).

46 Since the axis of Jupiter's magnetic field is tilted by ~ 10 degrees [Connerney *et al.*,
 47 1998, 2018] with respect to the rotational axis, the point of minimum centrifugal poten-
 48 tial along a magnetic field line is not in the plane of the rotational equator. Nor is it in the
 49 plane of the magnetic equator. Instead, the IPT lies in a plane tilted two-thirds of the way
 50 from the rotational equator to the magnetic equator, called the centrifugal equator [Hill
 51 *et al.*, 1974; Dessler, 1983; Khurana *et al.*, 2004]. Specifically, the axis of the centrifugal
 52 equator is tilted by ~ 7 degrees from the rotational axis and ~ 3 degrees from the mag-
 53 netic dipole axis. However, Jupiter's magnetic field is better represented by an offset tilted
 54 dipole. This magnetic equator is offset from the center of mass by approximately 0.119
 55 R_J at a latitude of 1.44 degrees and longitude of 150.2 degrees (System III left handed
 56 coordinate system) [Connerney, 1993; Weiss, 2004]. This is the "nominal" centrifugal
 57 equator that is based upon the offset tilted dipole approximation to Jupiter's magnetic field
 58 (OTD).

59 Yet observations suggest that the concept of a planar Io plasma torus and, by ex-
 60 tension, a planar centrifugal equator, is oversimplified [e.g., Schneider and Trauger, 1995;
 61 Herbert *et al.*, 2008]. Instead, the plasma torus appears "warped like a potato chip" [Her-
 62 bert *et al.*, 2008]. Such warping could be explained by the nature of Jupiter's magnetic

63 field. This can be pictured as follows, if Jupiter's magnetic field can be represented by a
 64 tilted dipole centered at Jupiter's center of mass, then the centrifugal equator is predicted
 65 to be a plane. However, higher-order moments in the magnetic field lead to higher-order
 66 structure in the surface of the centrifugal equator. This higher order structure leads to the
 67 plane of the centrifugal equator becoming perturbed from its planar shape. This is similar
 68 to the surface of a lake. With no disturbance the lake is a plane but if you add any per-
 69 turbation the surface deviates from its planar shape. Observations of the location of the Io
 70 plasma torus provide constraints on the magnetic field in the inner magnetosphere.

71 Three distinct regions of plasma exist within the torus [Bagenal and Sullivan, 1981;
 72 Bagenal, 1994; Thomas et al., 2004]. Each region has a distinct temperature and compo-
 73 sition. Moving outwards from Jupiter within the plane of the IPT, these regions are the
 74 cold torus, ribbon, and warm torus. The physical properties of the three torus regions
 75 are as follows [Bagenal and Sullivan, 1981; Bagenal, 1994; Schneider and Trauger, 1995;
 76 Schneider et al., 1997; Thomas et al., 2004; Steffl et al., 2006, 2008; Nerney et al., 2017;
 77 Bagenal et al., 2017b]. The cold torus is centered around $5.2 R_J$, contains mostly S^+ ions
 78 with lesser amounts of O^+ ions, has peak densities around 1000 cm^{-3} , ion temperatures
 79 around 2–4 eV, and a scale height $\sim 0.1 R_J$. The cold torus is thought to form by rapid ra-
 80 diative cooling of ions that diffuse towards Jupiter. The ribbon is centered around $5.6 R_J$
 81 , contains mostly O^+ ions with lesser amounts of S^+ ions, has peak densities around 3000
 82 cm^{-3} , has ion temperatures around 10–30 eV, and a scale height of $\sim 0.6 R_J$. The ribbon
 83 is visible as a narrow region of bright S^+ emissions in ground-based observations at opti-
 84 cal wavelengths. The warm torus has maximum densities at $5.9 R_J$ (Io's orbital distance),
 85 but extends outwards to $\sim 8 R_J$ (approaching Europa's orbit). It contains mostly S^{2+} and
 86 O^+ ions, has peak densities around 2000 cm^{-3} , has ion temperatures around 60 eV, and a
 87 scale height $\sim 1.0 R_J$. The warm torus region contains most of the plasma in the IPT.

88 The actual properties of the IPT vary from the reference description provided above.
 89 Particularly significant variations include spatial variations with System III longitude, tem-
 90 poral variations, and Io's orbital phase [Schneider et al., 1997; Nozawa et al., 2004; Steffl
 91 et al., 2006, 2008; Tsuchiya et al., 2015; Tsuchiya et al., 2019]. Variations with plasma
 92 supply and its effect on the system have been seen with the Hisaki spacecraft [Tsuchiya
 93 et al., 2018; Yoshioka et al., 2018].

94 In the ribbon, ion temperatures and associated scale heights vary strongly with Sys-
 95 tem III longitude. Maximum temperatures of 80 eV are seen at 80° longitude and mini-
 96 mum temperatures of 25 eV are seen at 200° longitude (note that these extrema are not
 97 180° apart). Cold torus ion temperatures are also found to vary with System III longitude
 98 [Schneider and Trauger, 1995; Schneider et al., 1997; Herbert et al., 2008]. There is no
 99 consensus [Thomas et al., 2004] on the cause of the observed variations with System III
 100 longitude, although the minimum in ion temperature roughly coincides with the maximum
 101 jovian surface magnetic field strength [Thomas et al., 2004]. It is generally thought that
 102 variations in Io plasma torus properties with System III longitude are controlled by varia-
 103 tions in the magnetic field environment.

104 Ground-based observations showed that on timescales of a year or so, the S^+ 673.1
 105 nm emission could vary by a factor of 4 [Thomas et al., 2004]. Furthermore, the rib-
 106 bon, while frequently by far the most prominent feature in optical images, was not always
 107 present [Thomas et al., 2004; Herbert et al., 2008]. Frequent routine ultraviolet observa-
 108 tions of the Io plasma torus by Cassini during its approach to Jupiter permitted studies
 109 of variability on shorter timescales [Steffl et al., 2004a,b, 2008]. Steffl et al. [2004a] found
 110 that over a period of about 50 days, the S^{3+}/S^{2+} emission ratio almost doubled while the
 111 S^+/S^{2+} ratio decreased by about 50%. During the same period the emitted power in the
 112 strongest EUV line (S^{2+} at 68.0 nm) almost halved [Thomas et al., 2004]. It is generally
 113 thought that temporal variations in Io plasma torus properties on relatively long timescales
 114 are controlled by temporal variations in the production and loss of gases at Io.

Based on the above discussion, it follows that precise observations of the locations, central densities, and scale heights of the distinct regions of the Io plasma torus over a range of System III longitudes would greatly improve characterization of the behavior of the torus. As discussed by *Phipps and Withers* [2017], the Juno spacecraft is uniquely suited to provide such observations from radio occultations of the Io plasma torus around perijove. Fortuitously, suitable measurements are routinely acquired by Juno during normal gravity science operations.

First results from Juno radio occultation observations on Perijove 1 were reported by *Phipps et al.* [2018]. The torus density distribution was accurately measured, and distinct torus regions were identified. *Phipps et al.* [2018] interpreted their results in terms of Voyager-era empirical density models and noted an offset between observed torus location and location predicted by an offset tilted dipole field model. However, a single occultation is not sufficient to characterize spatial and temporal variations in the density distribution of the torus. Therefore this article aims to report and interpret measurements of the density distribution in the Io plasma torus from subsequent Juno perijoves, specifically Perijoves 3, 6, and 8. Suitable data from subsequent perijoves are scheduled to be released on the NASA Planetary Data System in the future.

The structure of this article is as follows. Section 2 discusses the observing method used on Perijoves 3, 6, and 8, with emphasis on differences from the method used on Perijove 1. Section 3 presents the raw frequency data. Section 4 identifies, diagnoses, and resolves a problem in the raw data. Section 4 also generates the time series of torus total electron content values that are interpreted in subsequent sections. Section 5 compares total electron content observations to model predictions. Section 6 fits the total electron content observations to a simple function of distance above the nominal centrifugal plane, and finds best-fit values for peak total electron content, location offset, and scale height for distinct torus regions. Section 7 presents the interpretation of these best-fit values. Section 8 states the conclusions of this article.

2 Observational method

The basic geometry for each orbit is shown in Appendix A. During each Juno perijove, the Juno-Earth line of sight sweeps through one sector of the IPT. As time passes, the path of the line of sight through the IPT changes. As the spacecraft approaches perijove, the lines of sight begin to pass through the torus. Once the spacecraft passes through perijove, the lines of sight leave the torus. The received radio signals can be analysed to determine torus properties, since the plasma in the torus affects properties of the radio signals.

A suitable Juno-Earth radio link must be established in order to measure torus densities by radio occultations. This was accomplished on Perijoves (PJ) 1, 3, 6, and 8. Juno conducted microwave radiometer (MWR) observations in which Juno's high-gain antenna (HGA) was pointed away from Earth on PJ4, 5, 7, and 9 [*Buccino et al.*, 2018]. Juno was in safe mode on PJ2.

For PJ3, PJ6, and PJ8, Goldstone Deep Space Network (DSN) station DSS-25 transmitted X-band (7.2 GHz) and Ka-band (34 GHz) radio signals to Juno [*Buccino et al.*, 2018]. Juno then transmitted X-band (8.4 GHz) and Ka-band (32 GHz) radio signals back to Earth. The X-band downlink was referenced to the X-band uplink and the Ka-band downlink was referenced to the Ka-band uplink. Due to dispersion of the uplinked radio signals, the downlinked X-band and Ka-band signals are not coherently related. By contrast, for PJ1, Ka-band uplink was not used and the two signals transmitted by Juno were both coherently referenced to the X-band uplink.

In either case, the classical Doppler shift, relativistic effects, and the effects of Earth's neutral atmosphere can, in principle, be predicted using known trajectories and gravita-

165 tional fields, and accurate models of the troposphere, then subtracted from each received
 166 frequency to leave a quantity called the frequency residual [Withers *et al.*, 2014; Phipps
 167 and Withers, 2017]. At each band, this frequency residual should equal the frequency shift
 168 caused by the effects of plasma only. However, Jupiter's gravitational field and other non-
 169 gravitational effects are not known sufficiently well for this approach to be reliable (which
 170 is why Juno has a Gravity Science investigation). Instead, X-band and Ka-band observa-
 171 tions are analyzed together so that the non-dispersive (proportional to frequency, such as
 172 classical Doppler shift) and dispersive (not proportional to frequency, such as plasma ef-
 173 fects) effects can be separated.

174 To do this, the X- and Ka-band Doppler observables (f_{obs}) are combined to re-
 175 move the effects of plasma noise [e.g. Mariotti and Tortora, 2013], and adjustments are
 176 applied to the measurements to calibrate for Earth ionosphere from GPS data, and Earth
 177 troposphere from either analytical models or water vapor radiometer measurements (when
 178 available). Next, the spacecraft trajectory and Jupiter gravity field are estimated using the
 179 calibrated Doppler observables through statistical orbit determination, based on a Square
 180 Root Information Filter. The general orbit determination process is described in Tap-
 181 ley *et al.* [2004] and as applied to Juno in Folkner *et al.* [2017]. Third, the expected fre-
 182 quency (f_{comp}) is re-computed using the new estimated spacecraft trajectory and Jupiter
 183 gravity field from the orbit determination process. Finally, the residual frequency (δf) is
 184 computed individually for both X- and Ka-bands as the difference between the observed
 185 Doppler frequency (uncalibrated for plasma noise) and computed Doppler frequency:

$$186 \quad \delta f = f_{obs} - f_{comp} \quad (1)$$

187 Information about the total electron content is contained within the uncalibrated Doppler
 188 residuals.

189 The frequency residuals lead to torus density measurements. Specifically, Equation 2
 190 links these frequency residuals to the rate of change of the column electron content [Parisi
 191 *et al.*, 2018]:

$$192 \quad \Delta f = \delta f_{R,X} - \delta f_{R,Ka} \left(\frac{f_{D,X}}{f_{D,Ka}} \right) = \quad (2)$$

$$193 \quad \frac{e^2}{8\pi^2 m_e \epsilon_0 c f_{T,X}} \left(\left(M_{X,X}^2 + 1 \right) - \left(\frac{f_{D,X}}{f_{D,Ka}} \right)^2 \left(M_{Ka,Ka}^2 + 1 \right) \right) \frac{d}{dt} \int N dl$$

194 The first equality defines Δf , which is called the differential Doppler shift. Here Δf
 195 is the difference in frequency residuals, subscripts R and T refer to received and transmit-
 196 ted, respectively, subscript X refers to X-band, subscript Ka refers to Ka-band, c is the
 197 speed of light, t is time, l is distance along one leg of the two-way ray path, $-e$ is the
 198 electron charge, m_e is the electron mass, ϵ_0 is the permittivity of free space, and N is the
 199 electron density. Note that the integral is performed over one leg of the two-way ray path
 200 only, not both legs. It is assumed that the plasma contents along the uplink and down-
 201 link ray paths are identical. The individual frequency residuals are $\delta f_{R,X}$ and $\delta f_{R,Ka}$.
 202 The ratio $\frac{f_{D,X}}{f_{D,Ka}}$ is the ratio of the downlinked X-band frequency to the downlinked Ka-
 203 band frequency, equal to $\frac{880}{3360}$ [Asmar *et al.*, 2017]. $M_{X,X}$ is the spacecraft turnaround
 204 ratio for X-band uplink to X-band downlink, $\frac{880}{749}$, and $M_{Ka,Ka}$ is the turnaround ratio
 205 for Ka-band uplink to Ka-band downlink, $\frac{3360}{3599}$ [Asmar *et al.*, 2017]. Equation 2 applies
 206 to both the one-way observations of PJ1 and the two-way observations of PJ3, 6, and 8.
 207 In the one-way case of PJ1, $M_{Ka,Ka}$ is replaced with the turn-round ratio for X-band to
 208 Ka-band, $M_{X,Ka}$, $\frac{3360}{749}$. With this substitution, the right-hand side can be simplified to
 209 $\left(1 - \left(\frac{f_{D,X}}{f_{D,Ka}} \right)^2 \right)$. For PJ1, a simpler version also applies in which the frequency residuals

210 are replaced by the received frequencies (Equation 1 of *Phipps et al.* [2018]). This is eas-
 211 ier to use since it eliminates the need to find mHz frequency residuals on GHz frequen-
 212 cies, but it is not usable with incoherent two-way frequencies.

213 The basic analysis method, which was used by *Phipps et al.* [2018] for PJ1, is to
 214 take the observed time series of frequency residuals, integrate with respect to time, and
 215 use Equation 2 to find an initial time series of the total electron content, TEC, defined
 216 as $\int N dl$. This contains several contributions from sources other than the IPT, such as
 217 Earth's ionosphere and the solar wind, which should be removed from the initial time
 218 series of TEC. First, contributions from Earth's ionosphere are removed. Occultation of
 219 Juno by the IPT takes several hours. Hence the contribution of Earth's ionosphere to the
 220 observed TEC will change significantly over the duration of the observations. This is a
 221 routine contaminating factor in DSN radio science observations that is measured using ra-
 222 dio links to GPS satellites visible above the DSN stations. A standard DSN data product
 223 (ION files, e.g., http://atmos.nmsu.edu/PDS/data/jnogr1_1001/ANCILLARY/ION/) pro-
 224 vides Earth's ionospheric TEC along the line of sight to Juno. This contribution is sub-
 225 tracted from the initial time series of TEC to obtain the intermediate time series of TEC.
 226 Second, contributions from changes in the solar wind are removed from the intermediate
 227 time series of TEC. The intermediate time series of TEC still contains a contribution from
 228 changes in the TEC in the solar wind along the Juno-Earth line of sight. This is not di-
 229 rectly measurable. Instead, a high-order polynomial baseline is fitted to the intermediate
 230 TEC values at times outside the interval of the IPT occultation, then subtracted to yield
 231 the final time series of TEC. Note that observations are insensitive to the actual value of
 232 the solar wind TEC.

233 3 Data

234 Time series of the differential Doppler shifts for PJ3, PJ6, and PJ8 are shown in
 235 Figure 1. They can be compared to the equivalent plot for PJ1 (Figure 2 of *Phipps et al.*
 236 [2018]). As the line-of-sight total electron content should be approximately the same be-
 237 fore and after the occultation (i.e., no contribution from Io plasma torus), it follows from
 238 Equation 2 that the time integral of the differential Doppler shift from the start of the ob-
 239 servation to the end of the observation should be zero. That is, the area between the curve
 240 and the horizontal axis in Figure 1 should be the same above and below the axis. This
 241 prediction will not be perfectly satisfied due to changes in background conditions, but it
 242 was reasonably well-satisfied on PJ1. For PJ3, PJ6, and PJ8, however, this prediction was
 243 not satisfied well at all.

244 The consequences of this issue can be seen in the left panels of Figure 2, which
 245 show the intermediate TEC profiles (correction for Earth's ionosphere, but not for the
 246 solar wind) for PJ3, PJ6, and PJ8. The Io plasma torus is readily identifiable as a local
 247 maximum in each panel. In each occultation, the ending TEC value is about 50 TECU
 248 ($1 \text{ TECU} = 10^{16} \text{ electrons m}^{-2}$) different from the starting TEC value. By contrast, the
 249 equivalent offset was merely 20 TECU for PJ1 as illustrated in the middle panel of Fig-
 250 ure 3 of *Phipps et al.* [2018]. Moreover, there are clear differences between the pre-torus
 251 baseline and the post-torus baseline in each case, unlike for PJ1.

252 If a linear fit to the pre-torus baseline is subtracted from each intermediate TEC
 253 profile to give a "final" TEC profile, as shown in the right panels of Figure 2, then prob-
 254 lems persist. The ending TEC values differ from their expected value of zero by about 30
 255 TECU for PJ3 and PJ6. The ending TEC value is near zero for PJ8, but the implied struc-
 256 ture of the torus is extremely unrealistic. These results suggest two regions of plasma: one
 257 in the centrifugal equator with peak TEC of ~ 20 TECU and a scale height of about $0.7 R_J$
 258 and the other about $3 R_J$ above the centrifugal equator with similar peak TEC and a
 259 scale height of about $1.7 R_J$. This is highly implausible. In each of these three perijoves,

260 the shape of the IPT contribution relative to the background is clearly anomalous relative
261 to expectations and earlier results from PJ1.

262 4 Additional correction of data

263 It is clear that an issue negatively affects the PJ3, PJ6, and PJ8 observations that did
264 not affect the PJ1 observations, which used a different observing technique. We conclude
265 that a problem exists with our preliminary TEC profiles for PJ3, PJ6, and PJ8.

266 Close inspection suggests that the issue is somehow associated with perijove as the
267 intermediate TEC profiles (left panels of Figure 2) appear reasonable before perijove, but
268 not after perijove. There is no obvious association between the onset of this issue and the
269 time of the torus occultation. Note that the timing of the torus occultation changes rela-
270 tive to perijove due to the tilt of the axis of the torus (centrifugal axis) relative to Jupiter's
271 rotational axis.

272 Together, these observations suggest that the issue is associated with Juno's orbital
273 motion, not the Io plasma torus. Therefore we test a correction method. We assume that
274 the observed differential Doppler shift is related to the true differential Doppler shift as
275 $\Delta f_{\text{observed}} = \Delta f_{\text{true}} + \epsilon$, then attempt to constrain the correction term ϵ . We focus first on
276 PJ3, then test our findings on PJ6 and PJ8.

277 4.1 Development of correction term

278 The test uses a correction method of the form $\Delta f_{\text{observed}} = \Delta f_{\text{true}} + \epsilon$, where ϵ is
279 an as-yet-undetermined source of error. We first consider the characteristics that should
280 be possessed by our correction function ϵ . The correction function ϵ should: (A) have an
281 identical functional form for Perijoves 3, 6, and 8; (B) be largest around perijove; (C) be
282 small away from perijove; (D) be appropriately shaped in time; (E) be appropriately sized
283 in magnitude; and (F) be physically plausible. Also, it is desirable we understand why this
284 correction function is not necessary for PJ1 or for other radio science investigations (e.g.,
285 Cassini).

286 Initial investigations suggest that one viable possible correction function is:

$$287 \epsilon = k \frac{dV_{\text{LOS}}}{dt} \quad (3)$$

288 Here V_{LOS} is the line-of-sight velocity component. This putative correction function is
289 effectively equivalent to a correction function that is proportional to the rate of change of
290 received frequency. Figure 3, which shows dV_{LOS}/dt for PJ3, illustrates that this putative
291 correction function satisfies requirements (A), (B), (C), and (D).

292 Requirement (E) can be satisfied by appropriate selection of the constant k . Figure
293 4 shows a set of time series of the “revised” intermediate TEC profile for PJ3. Each panel
294 shows an intermediate TEC profile derived using Δf_{true} derived from $\Delta f_{\text{observed}}$ and the
295 correction term $k dV_{\text{LOS}}/dt$ for different values of k . A pre-torus baseline fit to TEC val-
296 ues before 16.44 hours is also shown on each panel. Results are plausible when the post-
297 torus TEC values lie close to the extrapolation of the pre-torus baseline. Figure 4 shows
298 that a unique solution exists for k that is approximately 0.5 s km^{-1} .

299 Figure 5 shows the “revised” final TEC profile for PJ3 in which the baseline is sub-
300 tracted from the “revised” intermediate TEC profile with $k = 0.5 \text{ s km}^{-1}$ to account for
301 changes in the solar wind conditions along the line-of-sight during the observations. Here
302 the independent variable time has been replaced by distance z above the centrifugal plane,
303 as defined more precisely in Section 6. Figure 5 also shows a single Gaussian fit to the
304 data. The peak TEC from the single Gaussian fit is $22.17 \pm 0.19 \text{ TECU}$ at 17.54 hours.
305 The peak TEC from the data is $23.24 \pm 4.71 \text{ TECU}$ with a peak time of 17.59 ± 0.19

306 hours. The resultant fit parameters are realistic, which builds confidence in the validity of
 307 this correction approach.

308 4.2 Evaluation of correction term

309 Correction by the addition of a term proportional to the rate of change of the line-
 310 of-sight velocity appears to work well. For PJ3, the derived TEC profile and associated fit
 311 parameters appear reasonable (Figure 6). Furthermore, as will be shown in Section 4.3,
 312 the same correction term gives reasonable results for PJ6 and PJ8 (Figures 7 and 8).

313 To explain the physical origin of this putative functional form for the error, we hy-
 314 pothesize that an error exists in the calibration of the delay time between the reference
 315 oscillator and the transmitter for the Ka-band uplink at the DSS-25 antenna, a 34-m an-
 316 tenna at the Goldstone Deep Space Network (DSN) complex [Buccino, 2019]. When com-
 317 bined with the large frequency ramp rate used for the uplink transmissions in these Juno
 318 observations, such an error would lead to an error in the frequency residuals of the func-
 319 tional form postulated here. The same error would affect PJ3, PJ6, and PJ8 since DSS-25
 320 is the only DSN antenna with Ka-band uplink capabilities. This error would not affect
 321 PJ1, whose coherent observations did not use Ka-band uplink. Few other planetary radio
 322 science investigations have used Ka-band uplink. Cassini is the most prominent exam-
 323 ple. However, Juno is a unique mission. Due to its highly elliptical orbit around the most
 324 massive planet in the solar system, with perijove barely above the planet's ionosphere, the
 325 acceleration it experiences around perijove is unprecedented for planetary spacecraft not
 326 conducting propulsive maneuvers. It accelerates from a Jupiter-relative speed of 22.8 km
 327 s^{-1} 4.5 hours before perijove to 55.8 km s^{-1} at perijove. Consequently, the rate of change
 328 of its Doppler-shifted frequency is also exceptionally large around perijove, much larger
 329 than for Cassini. Hence similar effects on Cassini observations would be much smaller.

330 As the putative correction term satisfies all the requirements imposed upon it, we
 331 conclude that it is valid and use it in the remainder of this work. Delay time tests were
 332 conducted at DSS-25 in November 2018. The results determine that the unusual behaviors
 333 seen in the PJ3, PJ6, and PJ8 observations are associated with ground equipment [Buccino,
 334 2019].

335 4.3 Final TEC profiles for PJ3, PJ6, and PJ8

336 We apply the stated correction term with $k = 0.5 \text{ s km}^{-1}$ to the observed differential
 337 Doppler shift, derive the initial TEC profile, correct the initial TEC profile for the con-
 338 tribution from Earth's ionosphere to obtain the intermediate TEC profile, and correct the
 339 intermediate TEC profile for the contribution from changes in the solar wind by subtract-
 340 ing a high-order polynomial baseline fit to obtain the final TEC profile (middle panel of
 341 Figures 6, 7, and 8). Periods where torus contributions are present are excluded from the
 342 baseline fit (Table 1). The final TEC profiles are shown in Figure 9. The equivalent figure
 343 for PJ1 is Figure 4 of Phipps *et al.* [2018]. Potential errors introduced by uncertainty in
 344 the value of k are discussed in Section 6. The three final TEC profiles appear reasonable.
 345 The times of perijove (highlighted) are not distinctive in any way in the TEC profiles. Fig-
 346 ure 9 also shows predicted TEC profiles from Model B of Phipps *et al.* [2018] (see Ap-
 347 pendix B:) and data-model residuals. Asymmetries between shapes of the ingress (pre-
 348 peak TEC) and egress (post-peak TEC) portions of a given observed TEC profile are com-
 349 mon. For instance, on PJ6, the ingress portion is steeper than the egress portion, while the
 350 opposite is true for PJ8. Similar trends are seen in the model profiles, which demonstrates
 351 that these asymmetries are caused by the evolution of the occultation geometry over the
 352 course of the observation. Steep portions are associated with perijove, which is reasonable
 353 as the spacecraft is moving fastest at that time.

354 5 Data-model comparison

355 Here we compare the observed TEC profiles to predictions from Model B of *Phipps*
 356 *et al.* [2018]. Observed and predicted peak TEC values and times are listed in Table 2.

357 5.1 Perijove 3

358 Perijove 3 occurred on December 11, 2016. Observed peak TEC values are 8 per-
 359 cent smaller than predicted peak TEC. The observed time of peak TEC is 0.06 hours ear-
 360 lier than predicted. Although this difference is smaller than the formal uncertainty in the
 361 observed time, the basic shape of the observed profile appears shifted earlier than predic-
 362 tions. Such time differences could be caused by displacement of the torus from its ex-
 363 pected position in the nominal centrifugal equator for the offset tilted dipole (OTD) ap-
 364 proximation to the magnetic field [*Phipps et al.*, 2018]. The observed wings of the torus
 365 are narrower than predicted, which suggests that the scale height of the warm torus is
 366 smaller than predicted. The absence of a narrow peak around the time of maximum TEC
 367 suggests that the cold torus does not contribute appreciably to the observed TEC.

368 5.2 Perijove 6

369 Perijove 6 occurred on May 19, 2017. The observed peak TEC is about 16 percent
 370 larger than predicted. The observed and predicted times of peak TEC differ by only 0.01
 371 hours. However, the basic shape of the observed profile appears shifted later than predic-
 372 tions. The observed and predicted wings of the torus have similar widths, which suggests
 373 that the scale height of the warm torus is similar to predictions. A narrow peak around
 374 the time of maximum TEC suggests an appreciable contribution from the cold torus to the
 375 observed TEC.

376 5.3 Perijove 8

377 Perijove 8 occurred on September 1, 2017. The observed TEC is about 28 percent
 378 larger than predicted. The observed and predicted times of peak TEC differ by only 0.01
 379 hours. However, the basic shape of the observed profile appears shifted earlier than predic-
 380 tions. The observed and predicted wings of the torus have similar widths, which suggests
 381 that the scale height of the warm torus is similar to predictions. A narrow peak around
 382 the time of maximum TEC suggests an appreciable contribution from the cold torus to the
 383 observed TEC. TEC fluctuations are noticeably larger for PJ8 than PJ1, PJ3, or PJ6. We
 384 consider two possible explanations: ionospheric conditions above the DSN ground station
 385 and the solar wind. PJ3 occurred shortly after local sunrise at the DSN station, PJ6 oc-
 386 curred at local nighttime, and PJ8 occurred during local mid-afternoon. Variations in true
 387 ionospheric conditions relative to the smooth ionospheric correction provided by DSN cal-
 388 ibration files are likely to have been greatest for the local mid-afternoon observations of
 389 PJ8. This appears as noise in the observed TEC profiles. Moreover, PJ8 occurred near so-
 390 lar conjunction when the Sun-Earth-Jupiter angle was 42.5 degrees, which gives a distance
 391 of the ray path of 6.1 astronomical units (AU). PJ3 and PJ6 had Sun-Earth-Jupiter angles
 392 of 61.6 and 135.4 degrees, respectively. As solar wind density decreases with increasing
 393 distance from the Sun, fluctuations in the solar wind contribution to TEC will increase as
 394 the Earth-Sun-Jupiter angle decreases [*Asmar et al.*, 2005]. These fluctuations, which will
 395 have been greatest for PJ8, appear as noise in the observed TEC profiles. Either explana-
 396 tion could be responsible for the disturbed fluctuations in the PJ8 TEC profiles.

397 5.4 Initial synthesis

398 Observed peak TEC values are roughly 20-40 percent greater than predicted on PJ1,
 399 PJ6, and PJ8, but about 10 percent smaller than predictions for PJ3. The basic shape of
 400 the observed TEC profile appears shifted earlier than predictions for PJ3 and PJ8, but later

401 for PJ1 and PJ6. The scale height of the warm torus appears consistent with predictions
 402 for PJ1, PJ6, and PJ8, but smaller than predicted for PJ3. The presence of the cold torus is
 403 apparent for PJ1, PJ6, and PJ8, but not for PJ3.

404 Displacement in time between the observed and predicted TEC profiles suggests dis-
 405 placement of the torus from the model's plane of the centrifugal equator, as discussed by
 406 *Phipps et al.* [2018] for PJ1. Variations in peak TEC value, warm torus scale height, and
 407 contribution by the cold torus suggest inherent variability in the density distribution of the
 408 torus. Possible causes include temporal variations associated with volcanic activity on Io
 409 and spatial variations associated with Jupiter's complex magnetic field, which is fixed in
 410 System III longitude.

411 6 Fit of two Gaussian functions to TEC data

412 In order to better interpret the initial impressions reported in Section 5.4, we fit the
 413 observed TEC profiles and consider the resultant fit parameters. Instead of fitting the ob-
 414 served TEC as a function of time, we fit TEC as a function of z . For each Earth received
 415 time, and hence each line of sight, z is defined as the z -coordinate of the point along the
 416 Juno-Earth line of sight whose value of $\sqrt{(x^2 + y^2)}$ equals $5.89 R_J$, the orbital distance of
 417 Io. Here x , y , and z are expressed in the centrifugal coordinate system introduced in sec-
 418 tion 2 of *Phipps et al.* [2018]. This position coordinate can be considered as the distance
 419 above the centrifugal equator at which the line-of-sight encounters the torus.

420 The data are now fit using the two Gaussian fit from *Phipps et al.* [2018]. This fit
 421 function is

$$422 TEC(z) = a_1 e^{-(z-b_1)^2/c_1^2} + a_2 e^{-(z-b_2)^2/c_2^2}, \quad (4)$$

423 where z is the distance from the centrifugal equator, a_n is the peak TEC, b_n is the peak
 424 location offset, and c_n is the scale height. This function is used with PJ3, PJ6, and PJ8
 425 to derive the peak TEC, peak location offset, and scale height for both the cold torus
 426 (smaller scale height, subscript 1) and torus beyond $5.5 R_J$ (larger scale height, subscript
 427 2). The ribbon and warm torus are combined into "the torus beyond $5.5 R_J$ " as the data
 428 are not sufficient to constrain a third Gaussian term [*Phipps et al.*, 2018].

429 The resulting fit parameters for PJ3, PJ6, and PJ8 are presented in Table 3. For each
 430 perijove, predicted, initial guess, and best-fit values of fit parameters are provided. Pre-
 431 dicted fit parameters come from a fit to Model B of *Phipps et al.* [2018] using appropriate
 432 geometry for each occultation. Initial guess fit parameters come from fitting the data us-
 433 ing the MatLab curve fitting routine. The best-fit values of fit parameters come from fit-
 434 ting the data using a Markov Chain Monte Carlo (MCMC) python routine that assumes a
 435 normal distribution for the parameters [*Foreman-Mackey et al.*, 2013] and uses the stated
 436 initial guesses. 10^5 runs were conducted for each perijove; the resultant best-fit values and
 437 their uncertainties are reported in Table 3. In order to account for possible errors in our
 438 adopted correction method, each run randomly selected a value for the correction term k
 439 from a uniform distribution between 0.45 and 0.55.

440 6.1 Perijove 3

441 The fit to PJ3 data is shown in Figure 10. The values of the fit parameters are shown
 442 in Table 3. For the cold torus, the peak total electron content is 62 ± 18 percent of the
 443 predicted value and the scale height is 86 ± 22 percent of the predicted value. For the
 444 torus beyond $5.5 R_J$, the peak total electron content is 97 ± 13 percent of the predicted
 445 value and the scale height is 81 ± 10 percent of the predicted value. The χ^2 for the fit
 446 was 0.10.

447 Parameters b_1 and b_2 indicate offsets in the fitted peak total electron contents from
 448 the OTD nominal centrifugal equator. Both predicted offsets are non-zero, even though the

model was defined to be symmetric about the centrifugal equator. Specifically, the peak offset values for the model are $-0.06 R_J$ for b_1 and $0.082 R_J$ for b_2 during PJ3. As discussed in *Phipps et al.* [2018], these non-zero values are artifacts of the geometry between the Juno-Earth lines-of-sight and the Io plasma torus. The lines-of-sight are not parallel to the OTD nominal centrifugal equator. When the PJ3 line of sight passes through the OTD nominal centrifugal equator at $\sqrt{x^2 + y^2} = 5.89 R_J$, the expected distance of peak density in the warm torus, Juno is at $\sqrt{x^2 + y^2} = 0.88 R_J$ and $z = 0.67 R_J$. Therefore this line of sight is at an angle of 7.6 degrees to the OTD nominal centrifugal equator. Consequently, the line of sight for which the model cold torus TEC is greatest passes through the OTD nominal centrifugal equator at a radial distance of $5.45 R_J$. Similarly the line of sight for which the model “torus beyond $5.5 R_J$ ” TEC is greatest passes through the OTD nominal centrifugal equator at a radial distance of $6.50 R_J$. As discussed below, these radial distances were used to infer the tilt of the torus.

Differences between predicted positions and best-fit positions (Table 3) indicate how observed torus regions are displaced from their expected locations. Δb_1 is $0.075 \pm 0.025 R_J$ for the cold torus and Δb_2 is $0.167 \pm 0.047 R_J$ for the torus beyond $5.5 R_J$. As discussed in *Phipps et al.* [2018], each offset can be related to the angular tilt of the observed plane of that torus region relative to the predicted plane in the OTD nominal centrifugal equator. Specifically, the angular tilt $\alpha_n = \arcsin\left(\frac{\Delta b_n}{R_n}\right)$. R_n is the radial peak location of the cold torus and the torus beyond $5.5 R_J$ (5.45 and $6.50 R_J$, respectively, as discussed above).

In this representation, a positive α_n corresponds to the observed plane of the torus being above the nominal centrifugal equator and a negative α_n corresponds to the observed plane of the torus being below the nominal centrifugal equator. *Phipps et al.* [2018] reported absolute values of tilts without emphasizing direction. Their inferred tilt values were negative (e.g., -1.6 degrees for the overall torus). For PJ3, we used the values stated above to find tilt angles α_n of 0.79 ± 0.26 degrees for the cold torus and 1.47 ± 0.41 degrees for the torus beyond $5.5 R_J$. If the two tilts are weighted by the fitted peak total electron content values, then the average tilt is 1.38 degrees. This is opposite in direction and 0.22 degrees smaller in magnitude than the tilt reported by *Phipps et al.* [2018] for PJ1.

6.2 Perijove 6

The fit to PJ6 data is shown in Figure 11. The values of the fit parameters are shown in Table 3. For the cold torus, the peak total electron content is 161 ± 20 percent of the predicted value and the scale height is 87 ± 10 percent of the predicted value. For the warm torus, the peak total electron content is 107 ± 13 percent of the predicted value and the scale height is 88 ± 11 percent of the predicted value. The χ^2 for the fit was 0.047.

The peak offset values for the model are $0.045 R_J$ for b_1 and $-0.021 R_J$ for b_2 during PJ6. When the PJ6 line of sight passes through the OTD nominal centrifugal equator at $\sqrt{x^2 + y^2} = 5.89 R_J$, the radial distance of the peak of the warm torus, Juno is at $\sqrt{x^2 + y^2} = 1.09 R_J$ and $z = -0.31 R_J$. Therefore this line of sight is at an angle of -3.6 degrees to the OTD nominal centrifugal equator. Consequently, the line of sight for which the model cold torus TEC is greatest passes through the OTD nominal centrifugal equator at a radial distance of $5.18 R_J$. Similarly the line of sight for which the model “torus beyond $5.5 R_J$ ” is greatest passes through the OTD nominal centrifugal equator at a radial distance of $6.22 R_J$.

Δb is $-0.017 \pm 0.010 R_J$ for the cold torus and Δb_2 is $-0.090 \pm 0.048 R_J$ for the torus beyond $5.5 R_J$. Using these values, we find tilt angles α_n of -0.19 ± 0.11 degrees for the cold torus and -0.91 ± 0.44 degrees for the torus beyond $5.5 R_J$. If the two tilts are weighted by the fitted peak total electron content values, then the average absolute

499 tilt is 0.72 degrees, which is 0.88 degrees smaller than the absolute angle of 1.6 degrees
500 found for PJ1 by *Phipps et al.* [2018].

501 6.3 Perijove 8

502 The fit to PJ8 data is shown in Figure 12. The values of the fit parameters are shown
503 in Table 3. For the cold torus, the peak total electron content is 235 ± 29 percent of the
504 predicted value and the scale height is 107 ± 10 percent of the predicted value. For the
505 warm torus, the peak total electron content is 107 ± 13 percent of the predicted value and
506 the scale height is 82 ± 9 percent of the predicted value. The χ^2 for the fit was 0.11.

507 The peak offset values for the model are $-0.082 R_J$ for b_1 and $0.102 R_J$ for b_2 dur-
508 ing PJ8. When the PJ6 line of sight passes through the OTD nominal centrifugal equa-
509 tor at $\sqrt{x^2 + y^2} = 5.89 R_J$, the radial distance of the peak of the warm torus, Juno is at
510 $\sqrt{x^2 + y^2} = 0.82 R_J$ and $z = 0.87 R_J$. Therefore this line of sight is at an angle of 9.7 de-
511 grees to the OTD nominal centrifugal equator. Consequently, the line of sight for which
512 the model cold torus TEC is greatest passes through the OTD nominal centrifugal equator
513 at a radial distance of $5.41 R_J$. Similarly the line of sight for which the model “torus be-
514 yond $5.5 R_J$ ” is greatest passes through the OTD nominal centrifugal equator at a radial
515 distance of $6.49 R_J$.

516 Δb is $0.005 \pm 0.011 R_J$ for the cold torus and Δb_2 is $0.122 \pm 0.068 R_J$ for the torus
517 beyond $5.5 R_J$. Using these values, we find tilt angles α_n of 0.05 ± 0.12 degrees for the
518 cold torus and 1.08 ± 0.60 degrees for the torus beyond $5.5 R_J$. If the two tilts are weighted
519 by the fitted peak total electron content values, then the average tilt is 0.72 degrees, which
520 is 0.88 degrees smaller than the absolute angle of 1.6 degrees found for PJ1 by *Phipps*
521 *et al.* [2018].

522 7 Discussion

523 The Juno radio occultations on PJ1, PJ3, PJ6, and PJ8 show some variability be-
524 tween the profiles. This variability could be due to System III longitude or time. Each
525 perijove provides a torus TEC profile at System III longitudes of 184, 60, 213, and 10 de-
526 grees, respectively. However, note that these stated System III longitudes correspond to
527 the longitude at which the line of sight crosses the OTD nominal centrifugal equator at
528 $\sqrt{x^2 + y^2} = 5.89 R_J$. Each occultation actually samples a range of longitudes as shown in
529 Table 4. We neglect this finite longitudinal extent in the analysis reported herein.

530 Figure 13 shows the observed angular tilts, fitted peak TEC values, and fitted scale
531 heights for each torus region and each perijove as functions of System III longitude. In
532 this section, we interpret the importance of System III longitude for each of these par-
533 ameters. *Hess et al.* [2011] discussed the System III longitude variations as being created by
534 variations in the hot electron populations interactions with the magnetic field. In the last
535 section we discuss the potential for temporal variability.

536 7.1 Angular tilt

537 In an analysis of ground-based optical observations, *Schneider and Trauger* [1995]
538 showed that the ribbon location was displaced from the centrifugal equator predicted by
539 an “offset tilted dipole” magnetic field model. The angular offsets found for the ribbon,
540 a part of the “torus beyond $5.5 R_J$ ”, by *Schneider and Trauger* [1995] are also shown in
541 the top panel of Figure 13 alongside the angular tilt results of this work. The angular tilt
542 of the cold torus found in this work matches the trend seen in ground-based observations
543 remarkably well. Although *Schneider and Trauger* [1995] use the O4 offset tilted dipole
544 (OTD), the difference between the *Phipps et al.* [2018] model with the VIP4 OTD and the
545 O4 OTD is negligible. The angular tilt of the torus beyond $5.5 R_J$ found in this work is

546 roughly consistent with the same sinusoidal trend and phasing, but has an amplitude ap-
 547 proximately 1.5–2 times greater. That is merely a general impression: the ratio of angular
 548 tilts between the two regions is not constant with longitude.

549 7.2 Peak total electron content

550 In an analysis of Cassini ultraviolet observations, *Steffl et al.* [2006] found temporal
 551 and azimuthal variations in the Io plasma torus electron densities. They found that the
 552 densities, for all regions together, varied sinusoidally with an amplitude of 5 percent and
 553 that peak density occurred at a System III longitude of 160 degrees. Considerable scatter
 554 existed around this trend, with many points displaced from this trend by up to 15 percent.
 555 The middle panel of Figure 13 adapts the density variation into TEC variations for the
 556 cold torus and torus beyond $5.5 R_J$. For the variation we use the median of the Juno fitted
 557 TEC, 23.2 TECU for the torus beyond $5.5 R_J$ and 8.2 TECU for the cold torus. The fitted
 558 peak TEC values for the torus beyond $5.5 R_J$ are consistent with the 5 percent variation
 559 and 160 degree phase of the density variations reported by *Steffl et al.* [2006], but they are
 560 also consistent with no variation with System III longitude. The outlier of PJ1 could be
 561 temporal and not spatial variability.

562 The fitted peak TEC values for the cold torus are not consistent with the amplitude
 563 and phase of the density variations reported by *Steffl et al.* [2006]. This is reasonable since
 564 the variations from *Steffl et al.* [2006] are for an averaged torus. The fitted values vary
 565 from around 3.25 TECU to 12.2 TECU (roughly 50–60 percent variation around the me-
 566 dian of 8.2 TECU). No smooth dependence on System III longitude is apparent for this
 567 parameter.

568 7.3 Scale height

569 Scale height is a proxy for the parallel ion temperature [Equation 6 of *Phipps et al.*,
 570 2018]. Variations in ground-based observations of parallel ion temperature with System III
 571 longitude have been discussed by *Brown* [1995], *Schneider and Trauger* [1995], *Schneider*
 572 *et al.* [1997], and *Herbert et al.* [2008]. They found that the parallel ion temperature var-
 573 ied sinusoidally as a function of System III longitude and the temperature variations were
 574 also different in the dawn and dusk ansae. For dusk observations of the ribbon, *Herbert*
 575 *et al.* [2008] found parallel ion temperatures to have a maximum at System III longitude
 576 of 30 degrees (50 eV) and a minimum at around 240 degrees (15–20 eV). For dawn ob-
 577 servations of the ribbon, *Herbert et al.* [2008] found parallel ion temperatures to have a
 578 maximum at System III longitude of 240 degrees (40 eV) and a minimum at around 120
 579 degrees (20 eV). For dusk observations of the cold torus, *Herbert et al.* [2008] found par-
 580 allel ion temperatures to have a maximum at System III longitude of 60 degrees (5 eV)
 581 and a minimum at around 240 degrees (2 eV). For dawn observations of the cold torus,
 582 *Herbert et al.* [2008] found parallel ion temperatures to have a maximum at System III
 583 longitude of 200 degrees (3.5 eV) and a minimum at around 60 degrees (2 eV).

584 The bottom panel of Figure 13 shows variations in scale heights found from Juno
 585 radio occultations with System III longitude. The Juno data come from the noon sector,
 586 not the dawn or dusk sectors accessible to ground-based observations.

587 For both the cold torus and the torus beyond $5.5 R_J$, the Juno scale heights have a
 588 maximum around 180 degrees System III longitude and a minimum around 60 degrees.
 589 However, the longitudinal resolution is extremely poor given four current occultations. The
 590 median scale height is $0.20 R_J$ for the cold torus and $0.92 R_J$ for the torus beyond $5.5 R_J$.
 591 With the average ion mass published in *Phipps et al.* [2018] we get a median ion tempera-
 592 ture of 2.7 eV for the cold torus and 52.15 eV for the the torus beyond $5.5 R_J$.

593

7.4 Temporal Variability

594 The Io plasma torus has been shown to vary temporally as well as with System III
 595 [Nozawa *et al.*, 2004; Steffl *et al.*, 2008; Schmidt *et al.*, 2018]. The time between two peri-
 596 joves is approximately 53 days.

597 Figure 14 shows the temporal variability between the perijoves. The time variability
 598 this probes is 106 days or longer. There are two time ranges. One time range is 106 days
 599 for PJ1–PJ3 and PJ6–PJ8. The other time span is from PJ3–PJ6 which is 159 days. It is
 600 difficult to tell if the variability seen here is temporal or System III variation. The offsets
 601 from dipolar are mostly affected by magnetic field geometry and therefore the variation
 602 shown here is mostly due to changes in System III. There is limited variability in the scale
 603 heights and densities in the torus $> 5.5R_J$. This variability could be either System III or
 604 temporal. The cold torus' TEC variations are larger than any shown before and are more
 605 likely related to temporal variations rather than any System III variability.

606

8 Summary and Conclusions

607 Juno conducted gravity science observations, including Io plasma torus radio oc-
 608 cultations, on Perijoves 1, 3, 6, and 8. Different observing modes were used on Perijove
 609 1 and Perijoves 3, 6, and 8. On Perijove 1, Juno transmitted coherent X-band and Ka-
 610 band signals referenced to an X-band signal uplinked from DSS-55 at Madrid [Folkner
 611 *et al.*, 2017; Phipps *et al.*, 2018]. In this mode, total electron content values could be de-
 612 termined directly from received frequencies. On Perijoves 3, 6, and 8, Juno transmitted
 613 non-coherent X-band and Ka-band signals. The X-band downlink was referenced to an
 614 X-band uplink from DSS-25 (Goldstone) and the Ka-band downlink was referenced to a
 615 Ka-band uplink from the same antenna. In this mode, total electron content values could
 616 only be determined from frequency residuals, which are much smaller and more challeng-
 617 ing to measure accurately. An error of some kind is present in the raw data products for
 618 Perijoves 3, 6, and 8. This is shown by the unphysical total electron content profiles that
 619 they produce. The error is eliminated by the incorporation of a correction term propor-
 620 tional to the rate of change of line-of-sight velocity between the antenna and Juno. This
 621 correction term is physically motivated and exactly the same correction yields satisfactory
 622 results for all three perijoves.

623 The angular offsets of torus regions from the nominal plane of the centrifugal equa-
 624 tor vary between the four perijoves. The angular offset of the torus beyond $5.5 R_J$ varies
 625 between -2 and 1 degrees. The angular offset of the cold torus varies less, between -1 and
 626 1 degrees. These variations appear controlled by System III longitude. We hypothesize
 627 that they may be caused by higher-order multipoles in the magnetic field structure, which
 628 distort the planar centrifugal equator predicted for a dipole field. The angular offset of the
 629 cold torus exhibits a clear sinusoidal dependence on System III longitude that is remark-
 630 ably similar to the dependence found for ground-based observations of the ribbon. The
 631 offsets found from the dipole model for the cold torus are consistent with those found by
 632 Schneider and Trauger [1995] for the ribbon. Herbert *et al.* [2008] found the ribbon offset
 633 from the cold torus positions.

634 Previous observations of the torus from Cassini [Steffl *et al.*, 2006] and Earth-based
 635 observatories [Schneider and Trauger, 1995; Schneider *et al.*, 1997; Nozawa *et al.*, 2004;
 636 Herbert *et al.*, 2008; Tsuchiya *et al.*, 2015] found the electron and ion density and temper-
 637 atures to vary sinusoidally with System III longitude. For Juno, the warm torus peak TEC
 638 varies with System III longitude, but does not appear to do so sinusoidally. However, fit-
 639 ted scale heights for both the cold torus and warm torus do vary with System III longitude
 640 in a manner that could be consistent with a sinusoidal variation.

641 Cold torus properties vary greatly between these Perijoves. The cold torus TEC,
 642 which can be considered proportional to peak density in this region, varies from a mini-

643 mum values of $3.25 \pm 0.93 \times 10^{16} \text{ m}^{-2}$ during PJ3 to a maximum values of 12.3 ± 1.50
 644 $\times 10^{16} \text{ m}^{-2}$ during PJ8. The scale height of the cold torus varies from a minimum value of
 645 $0.177 \pm 0.019 R_J$ during PJ6 to a maximum value of $0.348 \pm 0.051 R_J$ during PJ1.

646 By contrast, properties of the torus beyond $5.5 R_J$ do not vary as much between
 647 these perijoves. Three of the four peak TEC values are within about 10 percent of 23.2
 648 TECU. The outlier is PJ1, where the peak TEC is about 30 percent greater. The relevant
 649 scale heights vary from a minimum value of $0.878 \pm 0.091 R_J$ during PJ8 to a maximum
 650 value of $1.18 \pm 0.13 R_J$ during PJ1. All values are within 20 percent of $1 R_J$.

651 Radio occultations on Juno Perijoves 1, 3, 6, and 8 have sampled the density distri-
 652 bution in the Io plasma torus on four dates at intervals of several months. These obser-
 653 vations have occurred at System III longitudes around 30 degrees (PJ3, PJ8) and around
 654 200 degrees (PJ1, PJ6). Future observations on subsequent perijoves will provide improved
 655 temporal and longitudinal coverage.

656 A: Perijove 3, 6, and 8 trajectory

657 Figures 15, 16, and 17 present the trajectory of the Juno spacecraft during PJ3, PJ6,
 658 and PJ8, similar to Figure 1 from *Phipps et al. [2018]*. This gives an idea of the geometry
 659 of the lines of sight used for modeling the occultation. For each figure, cylindrical coor-
 660 dinates are used such that the vertical axis shows distance above the plane of the centri-
 661 fugal equator and the horizontal axis shows distance in the plane of the centrifugal equa-
 662 tor. The red disk at the origin shows Jupiter. Black triangles show the position of Juno at
 663 1000 second intervals. The apparent reversal of Juno's motion at $\pm 2 R_J$ above the cen-
 664 trifugal equator is not real; it is an artifact of the chosen coordinate system. Red dashed
 665 lines show lines-of-sight from Juno to Earth at the same intervals. The cyan dashed lines
 666 indicate the approximate times where the Juno lines of sight pass through the torus. The
 667 location of Juno for those lines of sight are indicated with blue circles. The shaded con-
 668 tours show IPT electron densities from Model B in *Phipps et al. [2018]*. In each figure,
 669 the motion of the Juno spacecraft is from the top to the bottom.

670 B: Model B parameters from *Phipps et al. [2018]*

671 The density distribution used in this paper is discussed in detail in *Phipps and With-*
 672 *ers [2017]* with updated parameters discussed in *Phipps et al. [2018]*. The equations for
 673 the distribution are:

$$N(R < 6.1R_J, r) = N_1 e^{-\frac{(R-C_1)^2}{(W_1)^2}} e^{-\frac{r^2}{H_1^2}} + \quad (\text{B.1})$$

$$N_2 e^{-\frac{(R-C_2)^2}{(W_2)^2}} e^{-\frac{r^2}{H_2^2}} +$$

$$N_3 e^{-\frac{(R-C_3)^2}{(W_3)^2}} e^{-\frac{r^2}{H_3^2}}$$

$$N(R > 6.1R_J, r) = N_4 e^{-\frac{(R-C_4)^2}{(W_4)^2}} e^{-\frac{r^2}{H_4^2}}. \quad (\text{B.2})$$

674 Here r is the distance perpendicular to the centrifugal equator, R is the radial distance
 675 from Jupiter, N_n is the central reference density (second column of Table 5), C_n is the ra-
 676 dial peak location (fifth column of Table 5), W_n is the radial width of each region ($0.2 R_J$
 677 for the cold torus, $0.08 R_J$ for ribbon, $0.32 R_J$ for warm torus, and $1.88 R_J$ for extended
 678 torus Gaussian), and H_n is the scale height (third column of Table 5). 1 refers to the cold
 679 torus, 2 to the ribbon, 3 to the warm torus, and 4 to an extended torus used to match the
 680 data beyond $6.1 R_J$. The parameterization of Model B is shown in Table 5.

Acknowledgments

The authors would like to thank Carl Schmidt for useful discussion related to the Io plasma torus variability. This work was supported in part by NASA award NNX15AI87G and 80NSSC19K0818. This work was partially carried out at the Jet Propulsion Laboratory, California Institute of Technology, under a contract with the National Aeronautics and Space Administration. The data used in this work are publicly available on the NASA Planetary Data System at http://pds-atmospheres.nmsu.edu/data_and_services/atmospheres_data/JUNO/gravity.html.

688 References

- 689 Asmar, S. W., J. W. Armstrong, L. Iess, and P. Tortora (2005), Spacecraft Doppler tracking: Noise budget and accuracy achievable in precision radio science observations, *Radio Science*, *40*, RS2001, doi:10.1029/2004RS003101.
- 690 Asmar, S. W., S. J. Bolton, D. R. Buccino, T. P. Cornish, W. M. Folkner, R. Formaro,
691 L. Iess, A. P. Jongeling, D. K. Lewis, A. P. Mittskus, R. Mukai, and L. Simone
692 (2017), The Juno Gravity Science Instrument, *Space Sci. Rev.*, *213*, 205–218, doi:
693 10.1007/s11214-017-0428-7.
- 694 Baggenal, F. (1994), Empirical model of the Io plasma torus: Voyager measurements, *J.
695 Geophys. Res.*, *99*, 11,043–11,062, doi:10.1029/93JA02908.
- 696 Baggenal, F., and J. D. Sullivan (1981), Direct plasma measurements in the Io
697 torus and inner magnetosphere of Jupiter, *J. Geophys. Res.*, *86*, 8447–8466, doi:
698 10.1029/JA086iA10p08447.
- 699 Baggenal, F., L. P. Dougherty, K. M. Bodisch, J. D. Richardson, and J. M. Belcher (2017a),
700 Survey of Voyager plasma science ions at Jupiter: 1. Analysis method, *J. Geophys. Res.
(Space Physics)*, *122*, 8241–8256, doi:10.1002/2016JA023797.
- 701 Baggenal, F., A. Adriani, F. Allegrini, S. J. Bolton, B. Bonfond, E. J. Bunce, J. E. P. Con-
702 nerney, S. W. H. Cowley, R. W. Ebert, G. R. Gladstone, C. J. Hansen, W. S. Kurth,
703 S. M. Levin, B. H. Mauk, D. J. McComas, C. P. Paranicas, D. Santos-Costa, R. M.
704 Thorne, P. Valek, J. H. Waite, and P. Zarka (2017b), Magnetospheric Science Objectives
705 of the Juno Mission, *Space Sci. Rev.*, *213*, 219–287, doi:10.1007/s11214-014-0036-8.
- 706 Brown, M. E. (1995), Periodicities in the Io plasma torus, *J. Geophys. Res.*, *100*, 21,683–
707 21,696, doi:10.1029/95JA01988.
- 708 Buccino, D., D. Kahan, O. Yang, and K. Oudrhiri (2018), Initial operations experience
709 and results from the Juno gravity experiment, in *2018 IEEE Aerospace Conference*, pp.
710 1–8, doi:10.1109/AERO.2018.8396438.
- 711 Buccino, D. R. (2019), Measurement of Station Delay at DSS-25, The In-
712 terplanetary Network Progress Report, Volume 42-217, pp. 1-11, May 15.
713 https://ipnpr.jpl.nasa.gov/progress_report/42-217/42-217B.pdf.
- 714 Connerney, J. E. P. (1993), Magnetic fields of the outer planets, *J. Geophys. Res.*, *98*, 18,
715 doi:10.1029/93JE00980.
- 716 Connerney, J. E. P., M. H. Acuña, N. F. Ness, and T. Satoh (1998), New models of
717 Jupiter's magnetic field constrained by the Io flux tube footprint, *J. Geophys. Res.*, *103*,
718 11,929–11,940, doi:10.1029/97JA03726.
- 719 Connerney, J. E. P., S. Kotsiaros, R. J. Oliversen, J. R. Espley, J. L. Joergensen, P. S. Joer-
720 gensen, J. M. G. Merayo, M. Herceg, J. Bloxham, K. M. Moore, S. J. Bolton, and S. M.
721 Levin (2018), A New Model of Jupiter's Magnetic Field From Juno's First Nine Orbits,
722 *Geophys. Res. Lett.*, *45*, 2590–2596, doi:10.1002/2018GL077312.
- 723 Dessler, A. J. (1983), *Physics of the Jovian Magnetosphere*, pp. 438–441, Cambridge, UK:
724 Cambridge University Press.
- 725 Folkner, W. M., L. Iess, J. D. Anderson, S. W. Asmar, D. R. Buccino, D. Durante,
726 M. Feldman, L. Gomez Casajus, M. Gregnanin, A. Milani, M. Parisi, R. Park, D. Serra,
727 G. Tommei, P. Tortora, M. Zannoni, S. J. Bolton, J. E. P. Connerney, and S. M. Levin
728 (2017), Jupiter gravity field estimated from the first two Juno orbits, *Geophys. Res. Lett.*,
729 44, doi:10.1002/2017GL073140.
- 730 Foreman-Mackey, D., D. W. Hogg, D. Lang, and J. Goodman (2013), emcee: The MCMC
731 Hammer, *Publ. A. S. P.*, *125*, 306–312, doi:10.1086/670067.
- 732 Herbert, F., N. M. Schneider, and A. J. Dessler (2008), New description of
733 Io's cold plasma torus, *J. Geophys. Res. (Space Physics)*, *113*, A01208, doi:
734 10.1029/2007JA012555.
- 735 Hess, S. L. G., P. A. Delamere, F. Baggenal, N. Schneider, and A. J. Steffl (2011), Lon-
736 gitudinal modulation of hot electrons in the Io plasma torus, *Journal of Geophysical
737 Research (Space Physics)*, *116*, A11215, doi:10.1029/2011JA016918.

- Hill, T. W., A. J. Dessler, and F. C. Michel (1974), Configuration of the Jovian magnetosphere, *Geophys. Res. Lett.*, 1, 3–6, doi:10.1029/GL001i001p00003.
- Khurana, K. K., M. G. Kivelson, V. M. Vasiliunas, N. Krupp, J. Woch, A. Lagg, B. H. Mauk, and W. S. Kurth (2004), *The configuration of Jupiter's magnetosphere*, pp. 593–616, Cambridge, UK: Cambridge University Press.
- Mariotti, G., and P. Tortora (2013), Experimental validation of a dual uplink multifrequency dispersive noise calibration scheme for Deep Space tracking, *Radio Science*, 48, 111–117, doi:10.1002/rds.20024.
- Nerney, E. G., F. Bagenal, and A. J. Steffl (2017), Io plasma torus ion composition: Voyager, Galileo, and Cassini, *J. Geophys. Res. (Space Physics)*, 122, 727–744, doi:10.1002/2016JA023306.
- Nozawa, H., H. Misawa, S. Takahashi, A. Morioka, S. Okano, and R. Sood (2004), Long-term variability of [SII] emissions from the Io plasma torus between 1997 and 2000, *J. Geophys. Res.*, 109, A07209, doi:10.1029/2003JA010241.
- Parisi, M., D. R. Buccino, and Y.-M. Yang (2018), Plasma noise calibration of two-way Doppler data, Jet Propulsion Laboratory, Pasadena, CA., Interoffice Memorandum, 332-DRB-20181018-19.
- Phipps, P. H., and P. Withers (2017), Radio occultations of the Io plasma torus by Juno are feasible, *J. Geophys. Res. (Space Physics)*, 122, 1731–1750, doi:10.1002/2016JA023447.
- Phipps, P. H., P. Withers, B. D. R., and Y.-M. Yang (2018), Distribution of plasma in the Io plasma torus as seen by radio occultation during Juno Perijove 1, *J. Geophys. Res. (Space Physics)*, 123, 6207–6222, doi:10.1029/2017JA025113.
- Schmidt, C., N. Schneider, F. Leblanc, C. Gray, J. Morgenthaler, J. Turner, and C. Grava (2018), A Survey of Visible S⁺ Emission in Io's Plasma Torus During the Hisaki Epoch, *Journal of Geophysical Research: Space Physics*, 123(7), 5610–5624, doi:10.1029/2018JA025296.
- Schneider, N. M., and J. T. Trauger (1995), The Structure of the Io Torus, *Astrophys. J.*, 450, 450, doi:10.1086/176155.
- Schneider, N. M., M. H. Taylor, F. J. Crary, and J. T. Trauger (1997), On the nature of the λ_{III} brightness asymmetry in the Io torus, *J. Geophys. Res.*, 102, 19,823–19,834, doi:10.1029/97JA00773.
- Steffl, A. J., A. I. F. Stewart, and F. Bagenal (2004a), Cassini UVIS observations of the Io plasma torus. I. Initial results, *Icarus*, 172, 78–90, doi:10.1016/j.icarus.2003.12.027.
- Steffl, A. J., F. Bagenal, and A. I. F. Stewart (2004b), Cassini UVIS observations of the Io plasma torus. II. Radial variations, *Icarus*, 172, 91–103, doi:10.1016/j.icarus.2004.04.016.
- Steffl, A. J., P. A. Delamere, and F. Bagenal (2006), Cassini UVIS observations of the Io plasma torus. III. Observations of temporal and azimuthal variability, *Icarus*, 180, 124–140, doi:10.1016/j.icarus.2005.07.013.
- Steffl, A. J., P. A. Delamere, and F. Bagenal (2008), Cassini UVIS observations of the Io plasma torus. IV. Modeling temporal and azimuthal variability, *Icarus*, 194, 153–165, doi:10.1016/j.icarus.2007.09.019.
- Tapley, B., B. Schutz, and G. Born (2004), Statistical Orbit Determination, *Elsevier*, pp. 50–56.
- Thomas, N., F. Bagenal, T. W. Hill, and J. K. Wilson (2004), The Io neutral clouds and plasma torus, in *Jupiter: The Planet, Satellites and Magnetosphere*, edited by F. Bagenal, T. E. Dowling, and W. B. McKinnon, pp. 561–591, Cambridge, UK: Cambridge University Press.
- Tsuchiya, F., M. Kagitani, K. Yoshioka, T. Kimura, G. Murakami, A. Yamazaki, H. Nozawa, Y. Kasaba, T. Sakanoi, K. Uemizu, and I. Yoshikawa (2015), Local electron heating in the Io plasma torus associated with Io from HISAKI satellite observation, *J. Geophys. Res. (Space Physics)*, 120, 10,317–10,333, doi:10.1002/2015JA021420.

- 794 Tsuchiya, F., K. Yoshioka, T. Kimura, R. Koga, G. Murakami, A. Yamazaki, M. Kagi-
795 tani, C. Tao, F. Suzuki, R. Hikida, I. Yoshikawa, Y. Kasaba, H. Kita, H. Misawa, and
796 T. Sakanoi (2018), Enhancement of the Jovian Magnetospheric Plasma Circulation
797 Caused by the Change in Plasma Supply From the Satellite Io, *J. Geophys. Res. (Space*
798 *Physics)*, 123(8), 6514–6532, doi:10.1029/2018JA025316.
- 799 Tsuchiya, F., R. Arakawa, H. Misawa, M. Kagitani, R. Koga, F. Suzuki, R. Hikida,
800 K. Yoshioka, A. Steffl, F. Bagenal, P. Delamere, T. Kimura, Y. Kasaba, G. Murakami,
801 I. Yoshikawa, A. Yamazaki, and M. Yoneda (2019), Azimuthal variation in the io
802 plasma torus observed by the hisaki satellite from 2013 to 2016, *J. Geophys. Res.*
(*Space Physics*), 124, doi:10.1029/2018JA026038.
- 803 Weiss, J. (2004), *Appendix 2: Planetary Parameters*, pp. 593–616, Cambridge, UK: Cam-
804 bridge University Press.
- 805 Withers, P., L. Moore, K. Cahoy, and I. Beerer (2014), How to process radio occultation
806 data: 1. From time series of frequency residuals to vertical profiles of atmospheric and
807 ionospheric properties, *Planet. Space Sci.*, 101, 77–88, doi:10.1016/j.pss.2014.06.011.
- 808 Yoshioka, K., F. Tsuchiya, M. Kagitani, T. Kimura, G. Murakami, D. Fukuyama, A. Ya-
809 mazaki, I. Yoshikawa, and M. Fujimoto (2018), The Influence of Io's 2015 Volcanic
810 Activity on Jupiter's Magnetospheric Dynamics, *Geophys. Res. Lett.*, 45(19), 10,193–
811 10,199, doi:10.1029/2018GL079264.
- 812

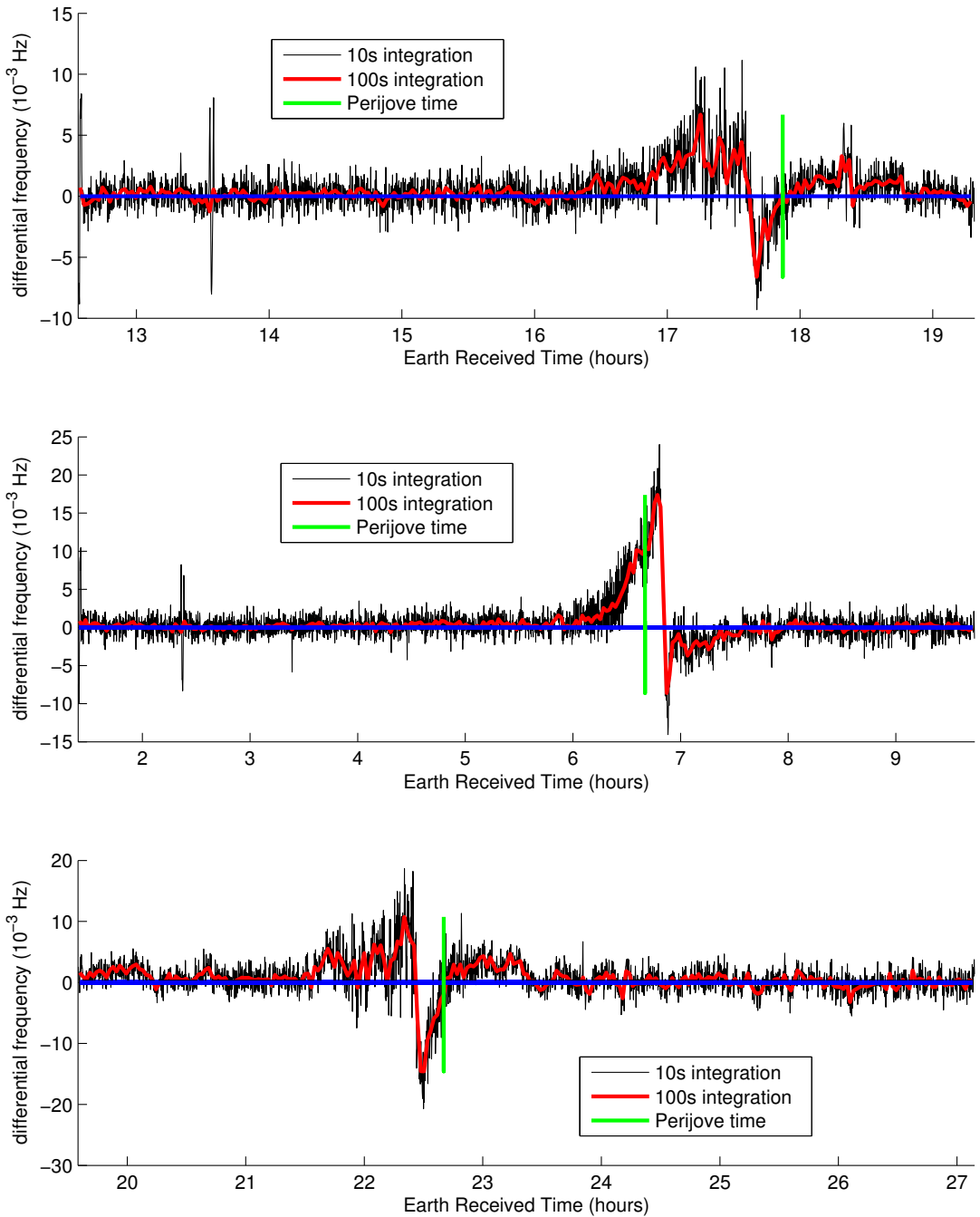


Figure 1. Time series of raw differential frequency shift for PJ3, PJ6, and PJ8

813

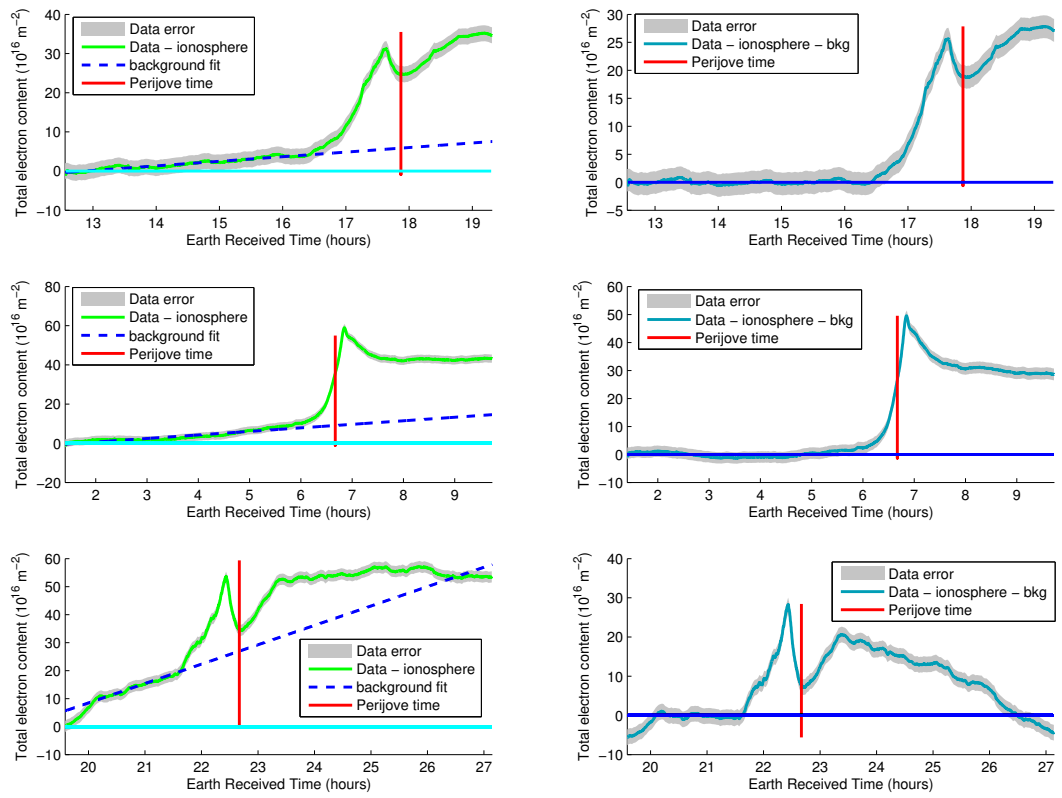


Figure 2. Preliminary versions of intermediate (left) and final (right) time series of total electron content for PJ3 (top), PJ6 (middle), and PJ8 (bottom).

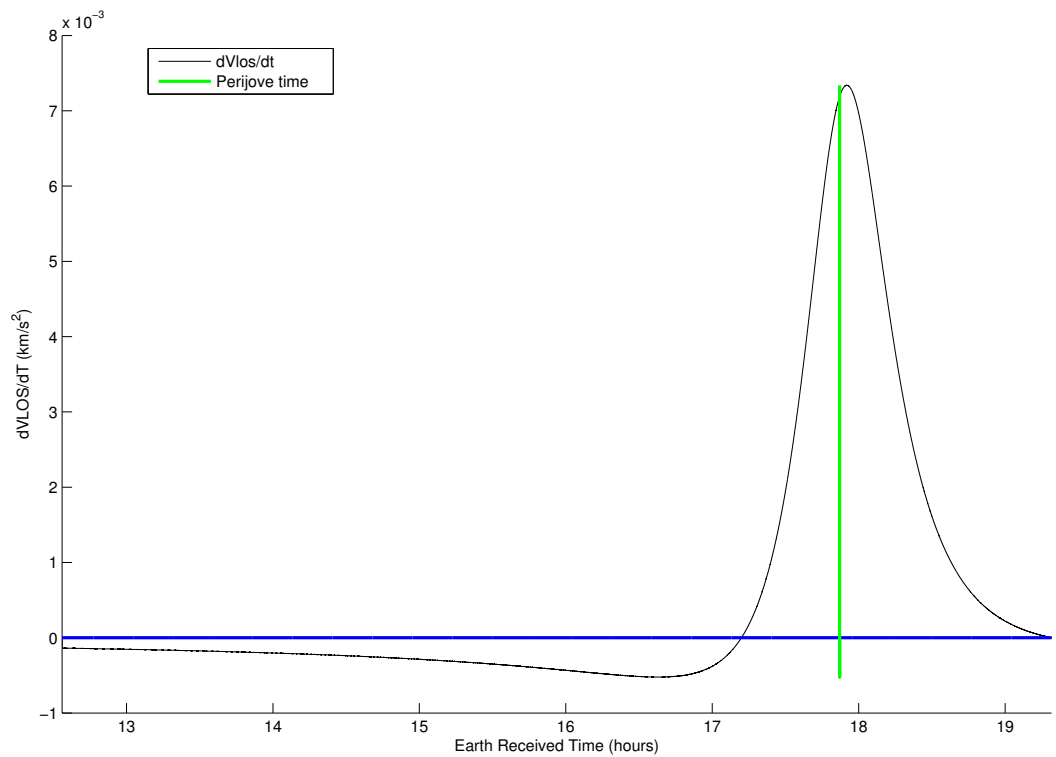
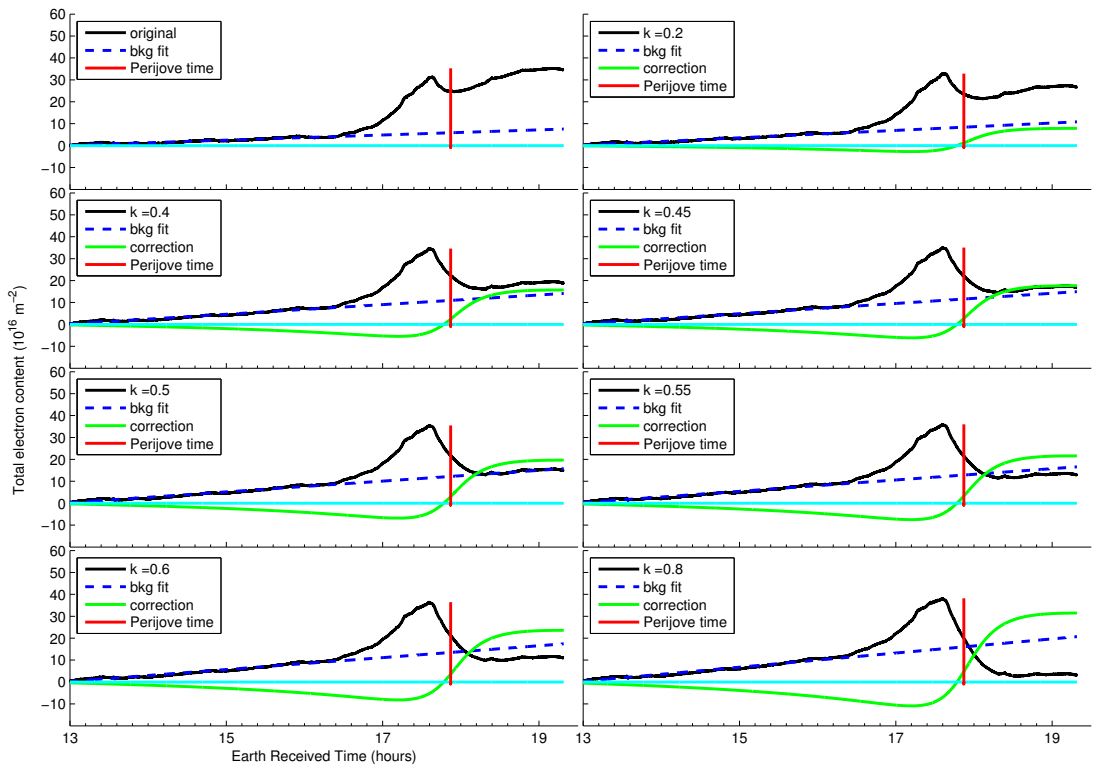


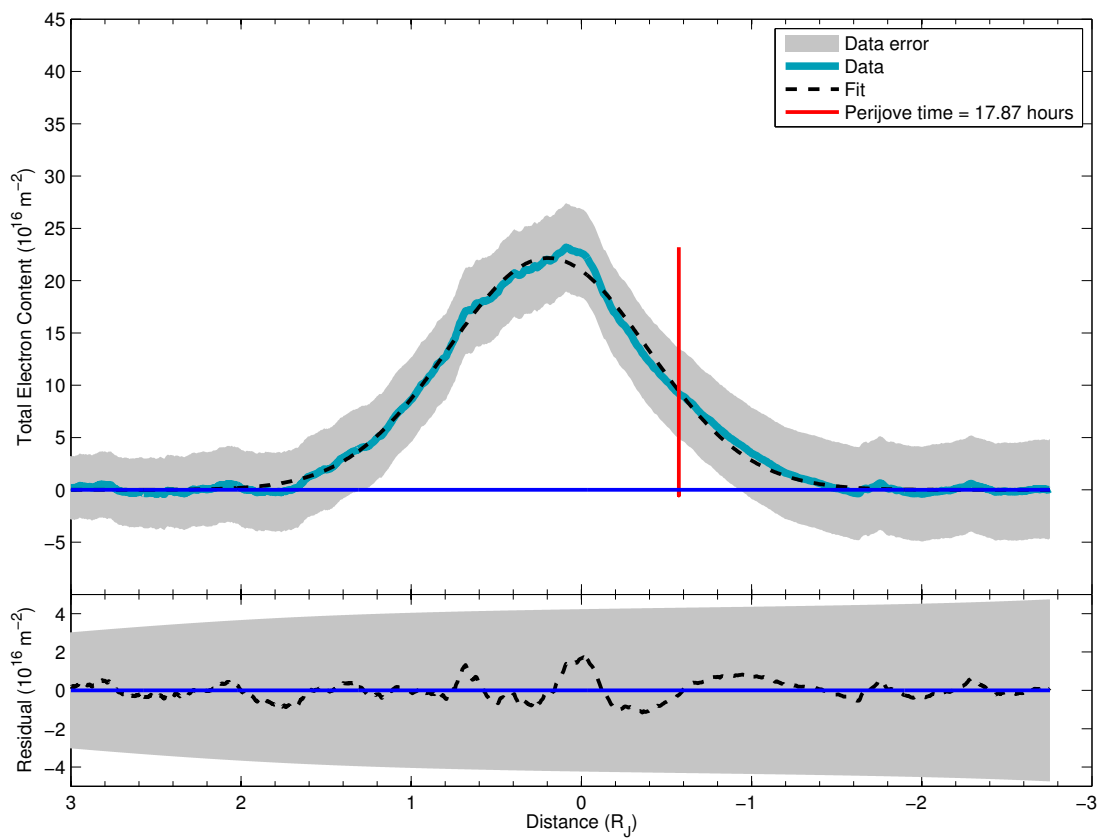
Figure 3. Line of sight velocity derivative for Perijove 3.



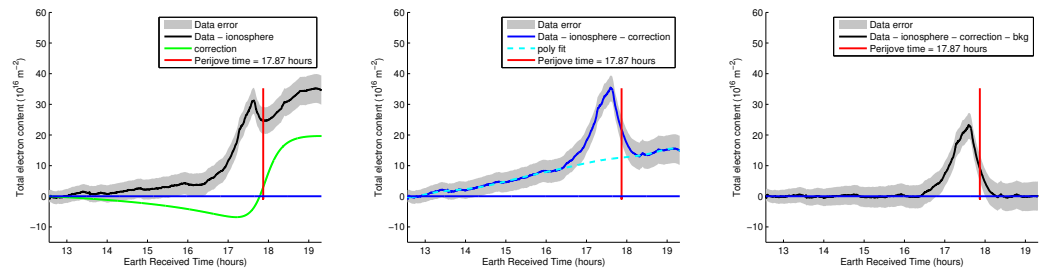
817 **Figure 4.** Corrected versions of intermediate time series of total electron content for PJ3 for $k = 0, 0.2, 0.4, 0.45, 0.5, 0.55, 0.6$ and 0.8 s km^{-1} . Finer resolution is provided around the optimal $k = 0.5 \text{ s km}^{-1}$.

818

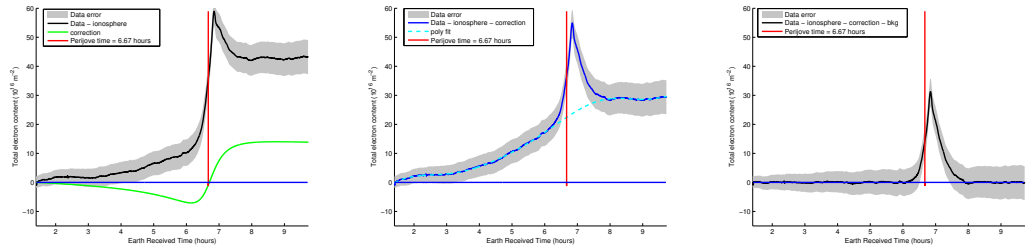
819



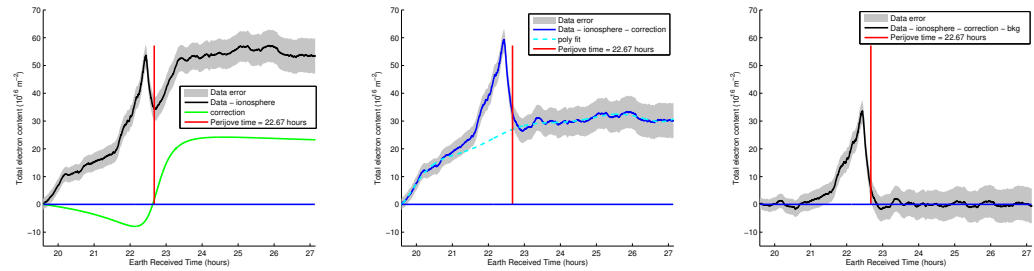
820 **Figure 5.** (top) Line of sight velocity corrected Perijove 3 total electron content with single Gaussian fit.
821 The red line indicates the time of perijove. (bottom) Residuals between single Gaussian fit and data.



822 **Figure 6.** Correction of the time series of total electron content for PJ3. (left) Line of sight velocity correc-
 823 tion,(middle) 9th order polynomial background fit, and (right) final corrected time series.



824 **Figure 7.** Correction of the time series of total electron content for PJ6. (left) Line of sight velocity correc-
 825 tion, (middle) 9th order polynomial background fit, and (right) final corrected time series.



826 **Figure 8.** Correction of the time series of total electron content for PJ8. (left) Line of sight velocity correc-
 827 tion, (middle) 9th order polynomial background fit, and (right) final corrected time series.

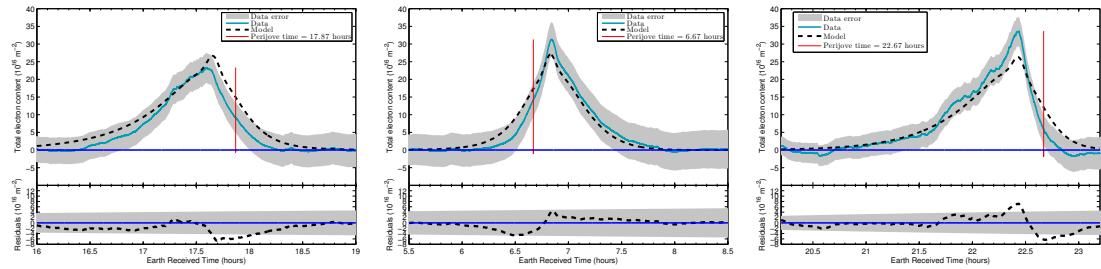
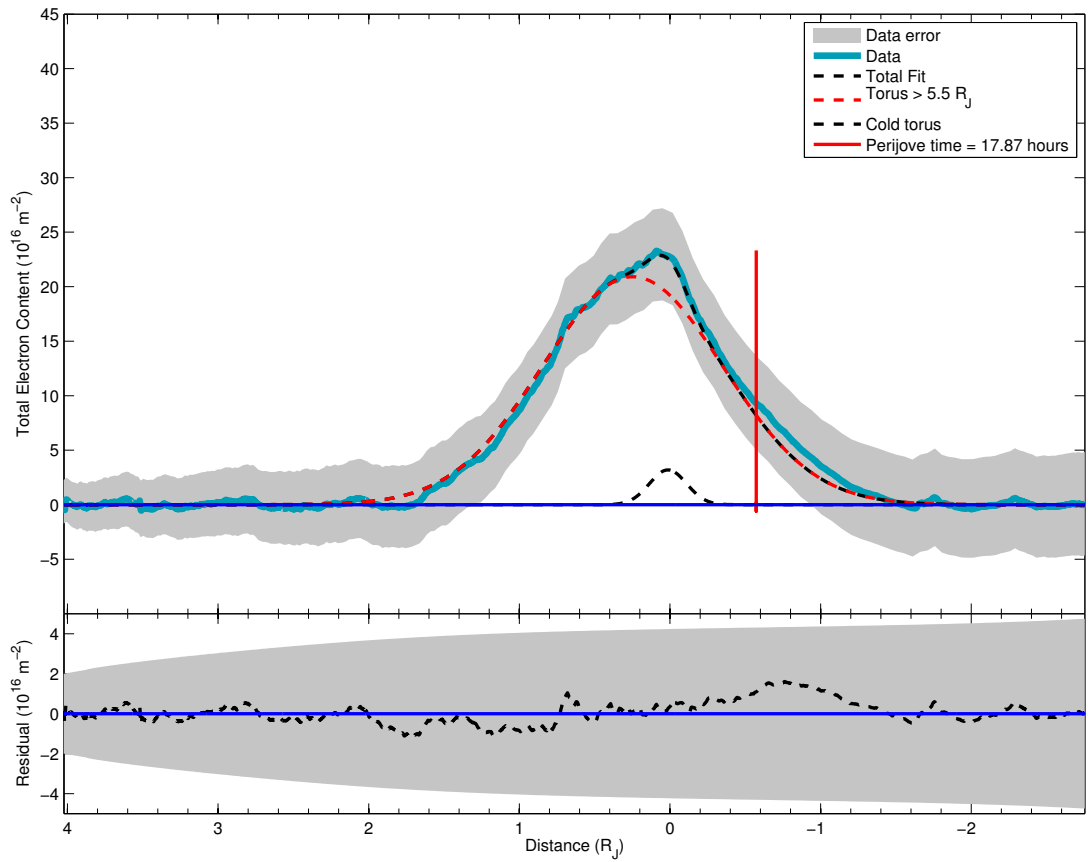
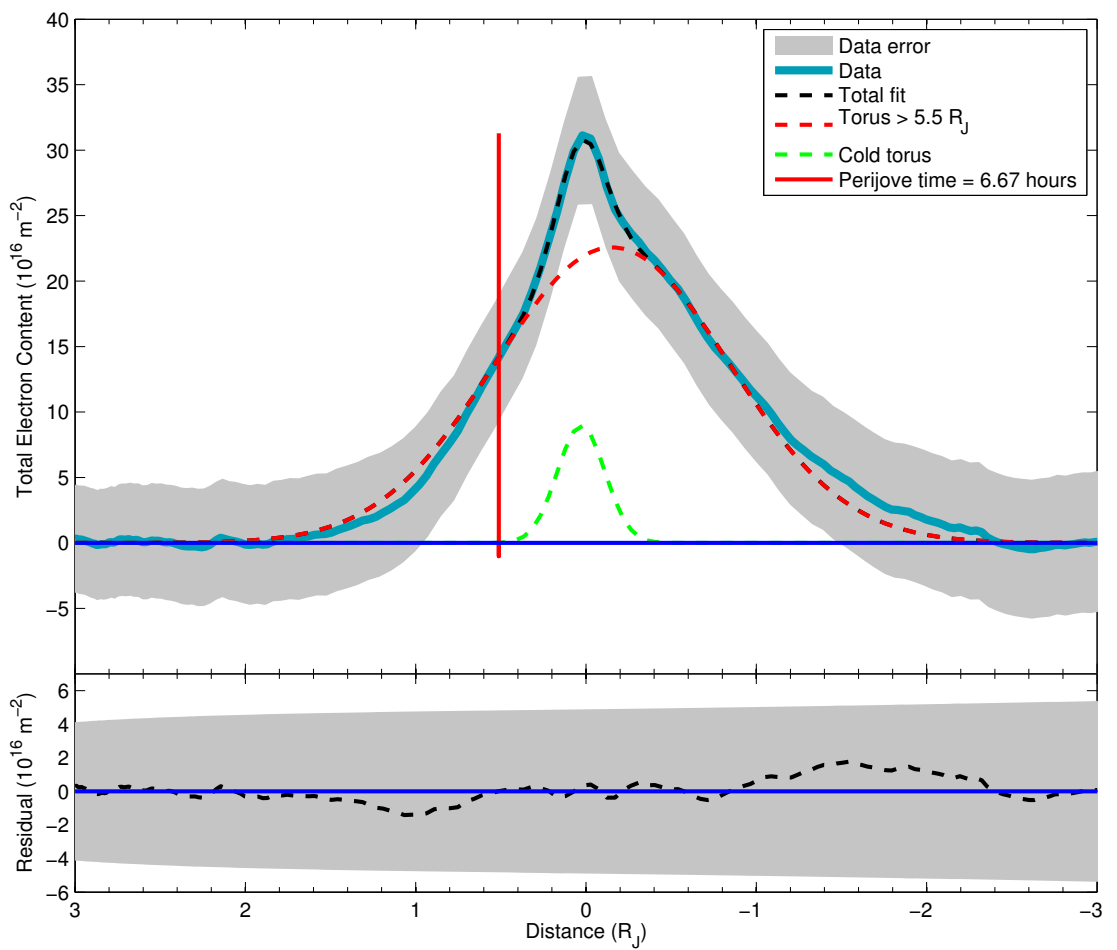


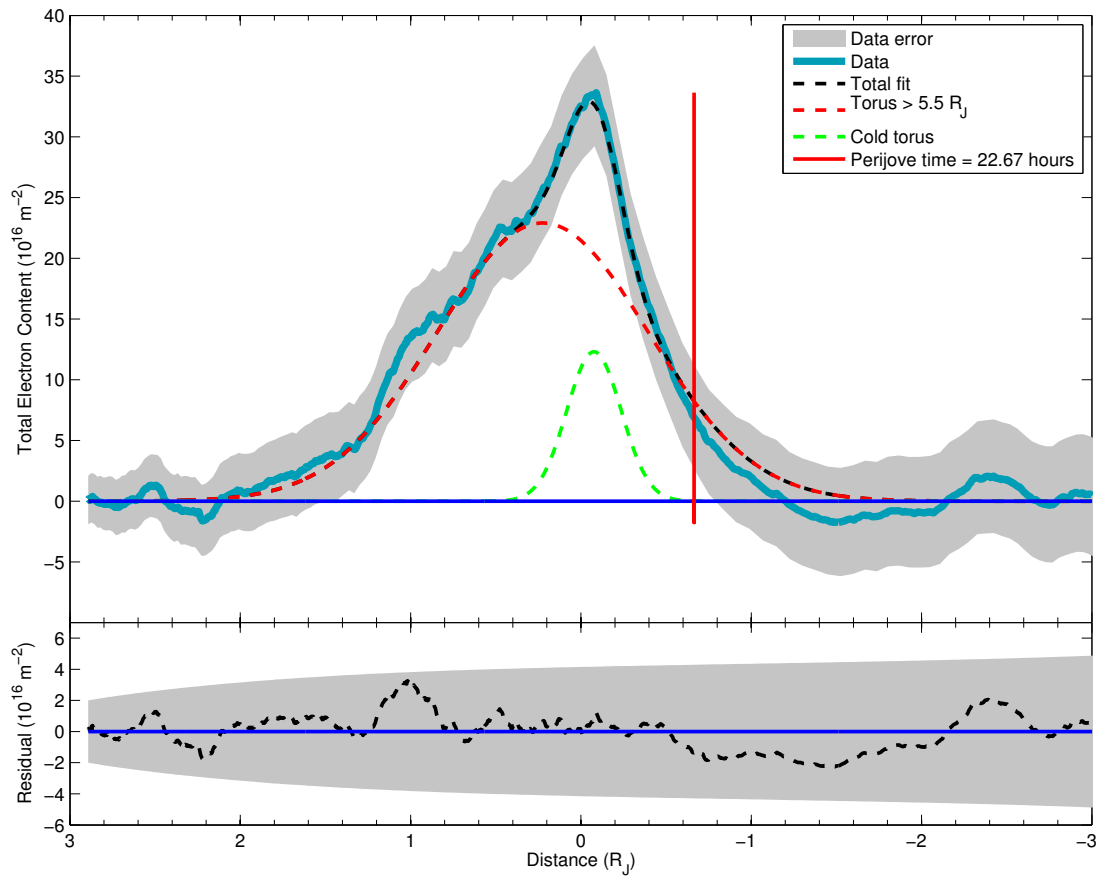
Figure 9. Corrected versions of final time series of total electron content for PJ3 (left), PJ6 (middle) and PJ8 (right) using $k = 0.5$. The bottom of each panel shows the residuals between data and model.
828
829



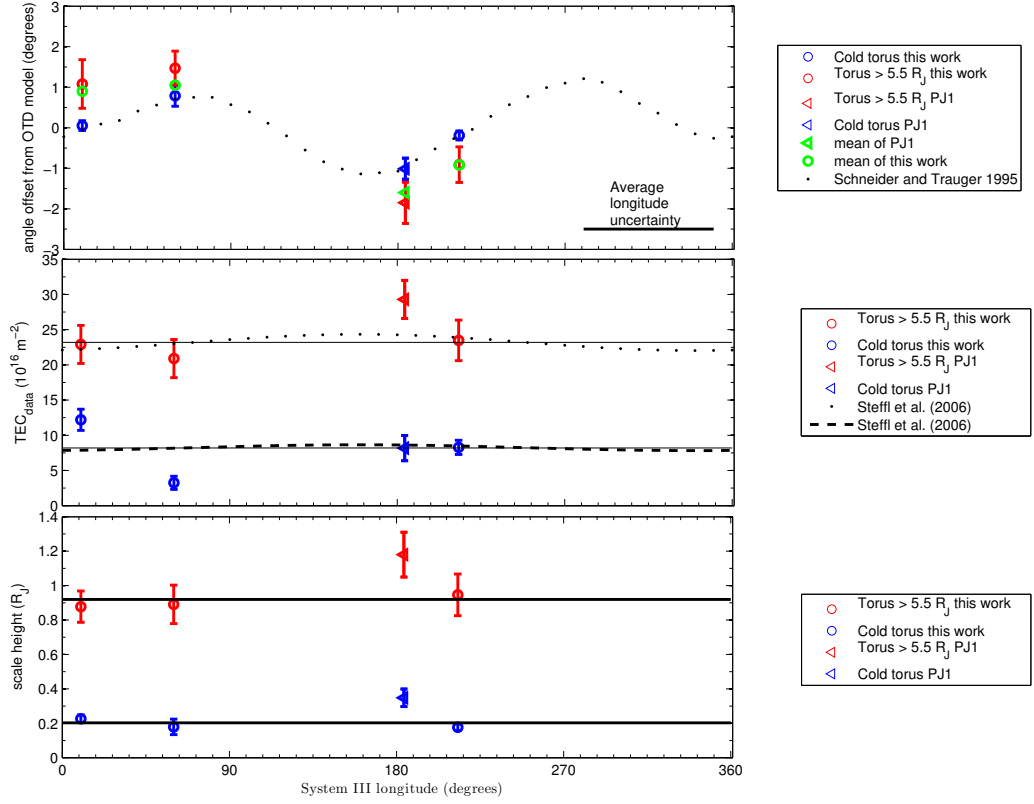
830 **Figure 10.** (top) Two Gaussian fit to the corrected final total electron content for PJ3 ($k = 0.5 \text{ s km}^{-1}$).
 831 (bottom) Residuals between data and fit.



832 **Figure 11.** (top) Two Gaussian fit to the corrected final total electron content for PJ6 ($k = 0.5 \text{ s km}^{-1}$).
833 (bottom) Residuals between data and fit.



834 **Figure 12.** (top) Two Gaussian fit to the corrected final total electron content for PJ8 ($k = 0.5 \text{ s km}^{-1}$).
835 (bottom) Residuals between data and fit.



836 **Figure 13.** (top) Dependence on System III longitude of angular offsets in locations of torus regions from
 837 nominal centrifugal equator. Blue, red, and green symbols show Juno radio occultation results for cold torus,
 838 torus beyond $5.5 R_J$, and their mean, respectively. These angular offsets are between the observed locations of
 839 these regions and the offset tilted dipole nominal centrifugal equator used in this work. The dotted line shows
 840 the angular offset of the ribbon relative to the offset tilted dipole nominal centrifugal equator. This is based on
 841 ground-based optical observations [Schneider and Trauger, 1995]. (middle) Dependence on System III longi-
 842 tude of fitted peak total electron content of torus regions. Blue and red symbols show Juno radio occultation
 843 results for the cold torus and torus beyond $5.5 R_J$, respectively. Horizontal lines show the median value of
 844 the Juno observations. Dashed and dotted lines show a prediction based upon Cassini ultraviolet spectrometer
 845 observations [Steffl et al., 2006]. (bottom) Dependence on System III longitude of fitted scale height of torus
 846 regions. Blue and red symbols show Juno radio occultation results for the cold torus and torus beyond $5.5 R_J$,
 847 respectively. Horizontal lines show the median values of the Juno observations.

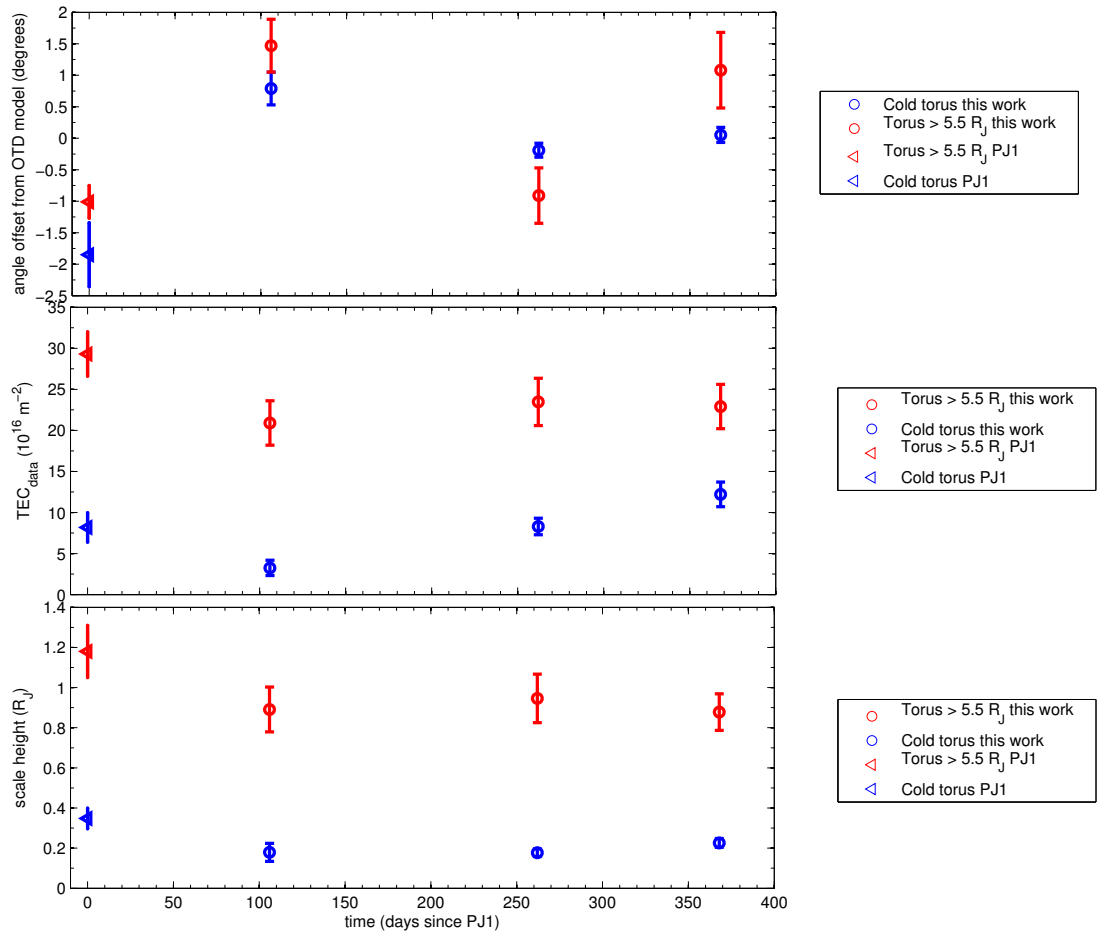


Figure 14. (top) Dependence on time for angular offsets in locations of torus regions from nominal centrifugal equator. (middle) Dependence on time for fitted peak total electron content of torus regions. (bottom) Dependence on time for fitted scale height of torus regions. (all) Blue and red symbols show Juno radio occultation results for the cold torus and torus beyond $5.5 R_J$, respectively.

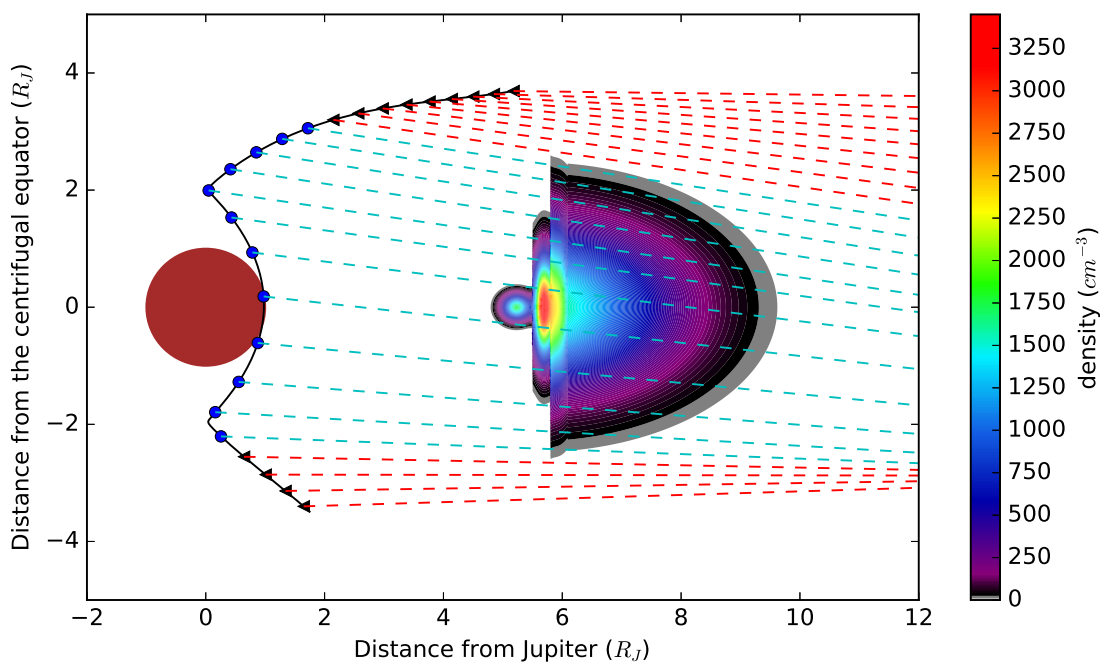
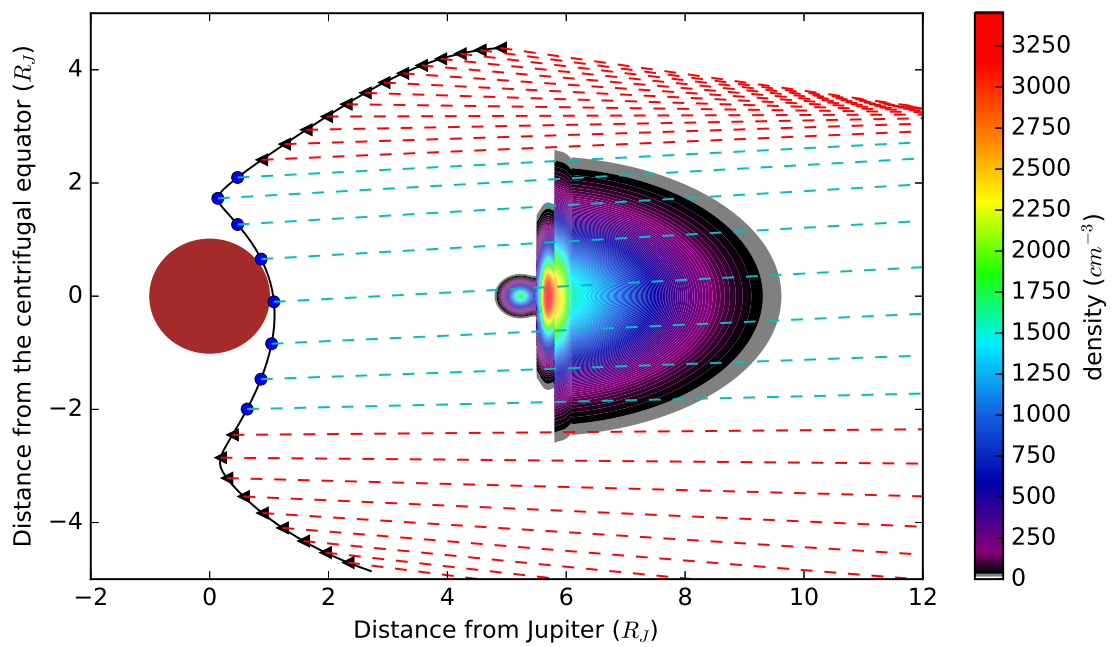
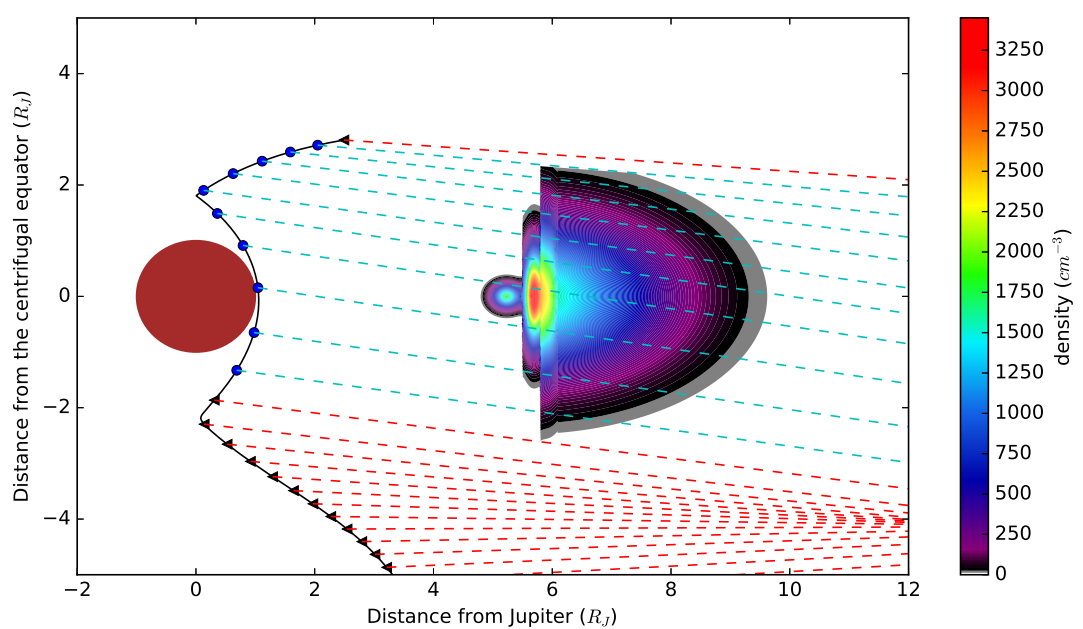


Figure 15. Illustration of the geometry of the PJ3 occultation of the Io plasma torus.



853

Figure 16. Illustration of the geometry of the PJ6 occultation of the Io plasma torus.



854

Figure 17. Illustration of the geometry of the PJ8 occultation of the Io plasma torus.

Table 1. Time periods excluded from baseline fit for Perijoves 3, 6, and 8.

Perijove	Torus start time UTC	Torus end time UTC
Perijove 3	16:23	18:23
Perijove 6	05:50	07:50
Perijove 8	20:58	22:58

856 **Table 2.** Observed and predicted time and value of maximum total electron content for PJ3, PJ6, and PJ8.
 857 Peak time is observed time of maximum total electron content. Peak TEC is observed value of maximum total
 858 electron content. Model time is predicted time of maximum total electron content in the Model B of *Phipps*
 859 *et al.* [2018]. Model TEC is predicted value of maximum total electron content in the Model B of *Phipps*
 860 *et al.* [2018].

Perijove	Date	peak time hours	peak TEC TECU	model time hours	model TEC TECU
Perijove 1	Aug 27, 2016	13.93 ± 0.02	36.8 ± 2.1	13.89	26.94
Perijove 3	Dec 11, 2016	17.59 ± 0.19	23.32 ± 4.71	17.65	26.64
Perijove 6	May 19, 2017	06.84 ± 0.04	31.29 ± 4.89	06.83	27.05
Perijove 8	Sept 1, 2017	22.44 ± 0.07	33.68 ± 4.17	22.43	26.30

861 **Table 3.** Parameters of two-Gaussian fit to observed TEC profiles. As discussed in the text, predicted values
 862 are from a model, initial guess values are from a preliminary fit to observations, and best-fit values are from a
 863 final fit to observations. PJ1 values are from a refit of data from *Phipps et al.* [2018].

Value	Peak TEC a_1 TECU	Cold torus			Torus $R > 5.5R_J$		
		Offset b_1 R_J	Scale height c_1 R_J	Peak TEC a_2 TECU	Offset b_2 R_J	Scale height c_2 R_J	
Perijove 1							
Best-fit	8.18 ± 1.80	-0.044 ± 0.024	0.348 ± 0.051	29.3 ± 2.7	-0.246 ± 0.056	1.18 ± 0.13	
Perijove 3							
Predicted	5.26	-0.060	0.209	21.6	0.082	1.10	
Initial guess	2.49	0.020	0.13	21.58	0.203	0.85	
Best-fit	3.25 ± 0.93	0.015 ± 0.025	0.179 ± 0.045	20.9 ± 2.7	0.249 ± 0.047	0.891 ± 0.112	
Perijove 6							
Predicted	5.16	0.045	0.204	21.9	-0.021	1.08	
Initial guess	8.95	0.028	0.196	22.66	-0.156	0.97	
Best-fit	8.29 ± 1.01	0.028 ± 0.010	0.177 ± 0.019	23.5 ± 2.9	-0.120 ± 0.048	0.946 ± 0.121	
Perijove 8							
Predicted	5.23	-0.082	0.210	21.5	0.102	1.07	
Initial guess	13.14	-0.070	0.24	22.38	0.25	0.95	
Best-fit	12.3 ± 1.5	-0.078 ± 0.011	0.226 ± 0.022	22.9 ± 2.7	0.224 ± 0.068	0.878 ± 0.091	

864 **Table 4.** Date, time, and System III longitude for Juno radio occultations. The start and end times corre-
 865 spond to the approximate Juno-Earth lines of sight encounters local density of more than 250 cm^{-3} in the Io
 866 plasma torus.

Perijove	Date	Torus Start time UTC	Torus Peak time UTC	Torus End time UTC	Torus Start λ_{III} degrees	Torus Peak λ_{III} degrees	Torus End λ_{III} degrees
Perijove 1	Aug 27, 2016	13:10	13:56	15:04	157	184	232
Perijove 3	Dec 11, 2016	16:38	17:38	18:18	37	60	100
Perijove 6	May 19, 2017	5:50	6:50	7:50	187	213	258
Perijove 8	Sept 1, 2017	21:24	22:24	23:24	348	10	48

867

Table 5. Parameters for Model B. $\langle M \rangle$ is mean ion mass.

Region	Reference Density [cm ⁻³]	Scale Height [R _J]	Ion Temperature [eV]	$\langle M \rangle$ [amu]	Peak Location [R _J]	Peak density [cm ⁻³]
Cold torus	1730	0.18	2.20	27.3	5.23	1740
Ribbon	2200	0.71	31.6	25.3	5.63	3240
Warm torus	2430	1.13	78.0	24.4	5.89	2430
Extended torus	2080	1.13	78.0	24.4	5.26	1740